



## Bed forms created by simulated waves and currents in a large flume

Jessica R. Lacy,<sup>1</sup> David M. Rubin,<sup>1</sup> Hiroshi Ikeda,<sup>2</sup> Kuniyasu Mokudai,<sup>2</sup> and Daniel M. Hanes<sup>1</sup>

Received 24 September 2006; revised 7 June 2007; accepted 2 July 2007; published 19 October 2007.

[1] The morphology and evolution of bed forms created by combinations of waves and currents were investigated using an oscillating plate in a 4-m-wide flume. Current speed ranged from 0 to 30 cm/s, maximum oscillatory velocity ranged from 20 to 48 cm/s, oscillation period was 8 s (except for one run with 12 s period), and the median grain size was 0.27 mm. The angle between oscillations and current was 90°, 60°, or 45°. At the end of each run the sand bed was photographed and ripple dimensions were measured. Ripple wavelength was also determined from sonar images collected throughout the runs. Increasing the ratio of current to wave (i.e., oscillatory) velocity decreased ripple height and wavelength, in part because of the increased fluid excursion during the wave period. Increasing the ratio of current to waves, or decreasing the angle between current and waves, increased the three-dimensionality of bed forms. During the runs, ripple wavelength increased by a factor of about 2. The average number of wave periods for evolution of ripple wavelength to 90% of its final value was 184 for two-dimensional ripples starting from a flat bed. Bed form orientations at the end of each run were compared to four potential controlling factors: the directions of waves, current, maximum instantaneous bed shear stress, and maximum gross bed form normal transport (MGBNT). The directions of waves and of MGBNT were equally good predictors of bed form orientations, and were significantly better than the other two factors.

**Citation:** Lacy, J. R., D. M. Rubin, H. Ikeda, K. Mokudai, and D. M. Hanes (2007), Bed forms created by simulated waves and currents in a large flume, *J. Geophys. Res.*, 112, C10018, doi:10.1029/2006JC003942.

### 1. Introduction

[2] The prediction of bed form morphologies produced by currents and waves is an important component of coastal sediment transport modeling, because of the strong influence of bottom roughness on resuspension dynamics. It is also important to the interpretation of bed forms found in the geologic record. Numerous field and laboratory studies have advanced the understanding of the relationship between wave forcing and ripple geometry, and, although significant uncertainty remains, numerous empirical predictive expressions for wave ripple wavelength and height have been proposed [e.g., Nielsen, 1981; Grant and Madsen, 1982; Wiberg and Harris, 1994; Mogridge et al., 1994; Xu and Wright, 1995; Styles and Glenn, 2002; Grasmeijer and Kleinhans, 2004; Williams et al., 2005]. Investigation of bed forms produced by noncolinear combinations of waves and currents has been much more limited, despite the frequent occurrence of such flows in coastal waters. Combined flows are difficult to produce in the laboratory, and the bed forms produced by combined flows include both 2D ripples and a

variety of three-dimensional (3D) bed forms, posing a more complex predictive problem than pure wave-generated ripples. Field studies of bed forms produced by waves and currents include those by Amos et al. [1988]; Li and Amos [1998]; Osborne and Vincent [1993]; Traykovski et al. [1999]; Hanes et al. [2001]; Smyth and Li [2005].

[3] Laboratory studies of ripples produced by combined flows have been conducted in wave-current basins and using oscillating plates. In addition, combinations of colinear waves and currents have been investigated in wave tunnels [e.g., Dumas et al., 2005; Cataño Lopera and Garcia, 2006]. Bagnold [1946] pioneered the use of an oscillating plate to simulate the influence of waves on the bed, reasoning that, in the reference frame of the plate, the fluid force on the grains on the plate is very similar to that produced by harmonic waves. Subsequent experiments with oscillating plates in the absence of current include those by Manohar [1955]; Sleath [1975]; Hansen et al. [2001]; Smith and Sleath [2005]. Lee Young and Sleath used a tray oscillating perpendicular to a steady flow to study bed forms [Lee Young and Sleath, 1990] and velocity profiles and bed shear stress [Sleath, 1990, 1991]. They found that straight-crested wave ripples become serpentine (wavy-crested) in the presence of a perpendicular current, and that the wavelength of the crest undulations scales with the product of the current and the wave period. Andersen and

<sup>1</sup>U.S. Geological Survey, Santa Cruz, California, USA.

<sup>2</sup>Terrestrial Environment Research Center, University of Tsukuba, Tsukuba, Japan.



**Figure 1.** (a) Flume and oscillating plate and (b) oscillating plate with instruments, at the end of run 16.

*Faraci* [2003] studied the formation of ripples in a wave basin with a current flowing at  $90^\circ$  to the wave direction. As the ratio of current strength to wave orbital velocity increased, ripples became serpentine, then segmented, and finally 3D. *Khelifa and Ouellet* [2000] investigated ripples formed by currents and waves at  $60^\circ$  or  $90^\circ$  using an intersecting wave flume and current channel, and found that ripple wavelength and height increased with current speed (see section 3.3). In work by both *Andersen and Faraci* [2003] and *Khelifa and Ouellet* [2000], wave periods never exceeded 1.4 s and the resulting bed forms were small.

[4] In this study we used an oscillating plate in a 4-m-wide flume to study bed forms produced by varying combinations of waves and currents. Because of the large width of the flume we were able to generate wave and current speeds and wave periods that are representative of field conditions. Our purpose was to investigate bed form categories, geometry, orientation, and evolution under steady forcing over a range of combinations of noncolinear waves and currents.

## 2. Methods

### 2.1. Experimental Apparatus and Procedures

[5] The experiments were conducted in the large flume (160 m  $\times$  4 m) at the Terrestrial Environment Research

Center of the University of Tsukuba in January 2005 (Figure 1a). To simulate wave velocities, a 2-m-diameter circular aluminum plate mounted on roller-blade wheels was driven back and forth across the flume. The speed of the motor driving the plate was controlled by a computer so that the velocity (and position) of the plate was sinusoidal, with amplitude and period specified for each run. The plate was driven by cables that passed through pulleys on the flume walls. Varying the position of the pulleys changed the angle between plate oscillation and current.

[6] Before each run, the plate was covered with a 10-cm flat bed of quartz sand. The sand had a median grain size  $D$  of  $1.91\phi$  (0.27 mm) and was moderately well sorted, with a standard deviation of  $0.53\phi$ . The sand bed was protected from flow disturbance by a shield of sheet metal while the flume was filled. Once the current had stabilized to the desired speed the shield was removed and plate oscillations commenced. Run length was approximately 40 min (Table 1). Water depth during all runs was 50 cm (35 cm above initial sand bed). The pumps creating the current were turned off approximately 1 min before the oscillations were stopped so that currents capable of transporting sand and oscillations stopped at about the same time. After each run the tank was drained very slowly (over about two hours) to prevent disturbance of the sand bed, and bed forms were measured and photographed. Distance across one or more

**Table 1.** Summary of Conditions During Experimental Runs<sup>a</sup>

Run	$d_{om}$ , cm	$T$ , s	$\bar{u}_n$ , cm/s	$\beta$ , deg	$u_b$ , cm/s	$d_o$ , cm	$\bar{u}$ , cm/s	$m$ , min	$Re_w \times 10^4$	$Re_p$	$Re_u \times 10^4$	$KC \times 10^3$	$\lambda$ , cm	$\eta$ , cm	BF
1	0	0	12	0	0	0	14.6	26	0	0	9.0	0	5.0	ND	C
2	60	8	12	90	30.7	78	14.6	51	12.0	83.0	9.0	9.1	10.0	1.0	IR
3	80	8	12	90	39.3	100	13.8	47	19.7	106.2	8.8	11.7	12.5	1.0	IR
4	100	8	12	90	47.0	120	14.2	39	28.1	126.8	8.3	13.9	14.0	2.5	IR
5	60	8	23	90	31.1	79	29.3	41	12.3	84.1	18.5	9.2	13.0	2.1	WC
6	80	8	23	90	39.2	100	30.4	38	19.6	105.9	19.0	11.6	15.0	1.7	WC
7	100	8	23	90	48.4	123	27.9	47	29.8	130.7	18.0	14.3	13.5	1.2	WC
8	60	8	36	90	33.6	86	46.3	17	14.4	90.7	29.4	10.0	ND	ND	C
9	60	8	6	90	29.1	74	7.2	46	10.8	78.6	4.5	8.6	14.0	2.0	LR
10	80	8	6	90	38.7	99	7.2	37	19.1	104.5	4.5	11.5	19.0	4.3	3D
11	80	8	0	0	38.2	97	0	38	18.6	103.2	0	11.3	17.5	3.4	IR
12	100	12	6	90	32.1	123	7.2	43	19.7	86.7	4.6	14.2	11.0	1.8	IR
13	60	8	12	90	30.1	77	14.8	40	11.6	81.3	9.3	8.9	12.5	2.0	IR
14	80	8	12	90	39.6	101	14.8	32	20.0	106.9	9.1	11.7	16.0	2.6	IR
15	100	8	6	90	48.3	123	8.2	53	29.7	130.4	5.0	14.3	24.0	5.0	3D
16	60	8	12	60	30.3	77	13.7	37	11.7	81.7	8.7	9.0	11.5	2.1	IR
17	40	8	12	60	21.7	55	14.2	40	6.0	58.7	9.2	6.4	8.4	1.3	WC
18	40	8	15	60	22.6	58	17.1	37	6.5	61.0	11.5	6.7	8.0	1.9	T
19	100	8	0	0	44.0	112	0	41	24.7	118.9	0	13.0	20.2	3.7	IR
20	40	8	12	45	21.8	55	12.3	39	6.0	58.8	8.4	6.5	9.0	1.3	T
21	60	8	12	45	27.2	69	12.0	38	9.5	73.6	7.9	8.1	8.8	1.5	T

<sup>a</sup>Here  $d_{om}$  is the excursion distance of the oscillating plate,  $T$  is the oscillation period,  $\bar{u}_n$  is the nominal depth-averaged current upstream of the plate, and  $\beta$  is the angle between the current and the plate oscillation;  $u_b$  is the amplitude of the measured wave velocities, calculated as  $\sqrt{2} u_{wRMS}$ , where  $u_w$  is the ADV velocity along the axis of plate motion,  $d_o$  is the orbital diameter calculated from  $u_b$ , and  $\bar{u}$  is the depth-averaged along-flume current calculated from the ADV velocity;  $m$  is run duration;  $Re_w = A u_b/\nu$  is the wave Reynolds number,  $Re_p = Du_b/\nu$  is the particle Reynolds number,  $Re_u = h\bar{u}/\nu$  is the flow Reynolds number, and  $KC = u_b T/D$  is the Keulegan Carpenter number, where  $\nu$  is kinematic viscosity,  $A = d_o/2$  is wave orbital amplitude,  $D$  is median grain size, and  $h$  is water depth. Ripple wavelength  $\lambda$  and height  $\eta$  are averages of physical measurements at the end of each run. Bed form (BF) categories are linear ripples (LR), irregular ripples (IR), wave and current ripples (WC), tiled (T), irregular three-dimensional (3D), and current (C). ND indicates no data.

series of 4–7 adjacent crests was measured with a meter stick or tape to determine average wavelength. Trough to crest ripple height was measured for at least 5 ripples. When there was more than one set of crests with different orientations ripple dimensions were measured for each trend. Ripple dimensions were measured in the downstream interior portion of the plate, where bed forms were relatively uniform and did not appear to be influenced by edge effects.

[7] Instruments mounted on a frame over the plate monitored conditions during each run (Figure 1b). Two fan-beam sonars (Imagenex 881A) were mounted 10 cm above the bed on the two downstream legs of the frame. The sonars scanned a sector of approximately  $108^\circ$  with a 2-m range, covering the entire plate, continuously during each run. The sonars completed a sweep approximately every 30 s. An acoustic Doppler velocimeter (ADV) sampling 6 cm above the bed was mounted near the center of the plate, and after run 10 a second ADV was added 54 cm across the plate from the first, sampling 16 cm above the bed. The ADVs sampled three components of velocity at 10 Hz continuously except for a 20 s interval every 15 min. The three transducers (1.0, 2.5, and 5.0 MHz) of an AquaScat acoustic backscatter sensor (ABS) were mounted approximately 30 cm above the bed on the stem of the first ADV. The ABS sampled backscatter intensity in 1-cm vertical bins at 8 Hz. The ABS electronics and logger were on the top of the instrument frame, the ADV loggers were mounted above the flume, and the sonars recorded directly to computers. The ABS data and suspended sediment dynamics will be discussed in another paper.

[8] Previous studies of wave simulation by oscillating plates have shown both experimentally and analytically that, in the frame of reference of the plate, velocity profiles in the

bottom boundary layer are essentially equivalent to those under waves of infinite length [Sleath, 1990, 1991]. The fluid forces on sediment grains are not identical for the two cases. The predominant horizontal forces on grains on an oscillating plate and under waves are a drag force, which is the same in the two cases, and an accelerative force [Nielsen, 1992; Madsen, 1991]. The accelerative force is caused by the pressure gradient under a surface wave, and by the plate motion on an oscillating plate. The ratio of the accelerative force under a wave to that on an oscillating plate is  $(1 + C_M)/(s + C_M)$ , where  $C_M$  is the added mass coefficient and  $s$  is the relative density of sediment [Nielsen, 1992]. This ratio is approximately 0.5 for spherical quartz sediment grains. The greater accelerative force for the oscillating plate is significant to sediment transport when the accelerative force is comparable to or larger than the drag force, which was not the case in our experiments (see section 3.1).

[9] Because the oscillating plate was above the floor of the flume, we expect that the current boundary layer was not fully developed over the plate, particularly in the upstream portion. The plate was driven sinusoidally, but the resulting motions were not perfectly sinusoidal, owing to friction, inertia, and cable stretching. Finally, the oscillations of the sand bed and instrumented frame produced complex three-dimensional flow disturbances (see section 3.1) which are not included in our analysis.

## 2.2. Processing of Sonar Data

[10] Ripple wavelength and orientation were determined from the sonar images using two-dimensional Fourier decomposition. Averaged backscatter intensities (in volts) from each sequential pair of sweeps were interpolated onto

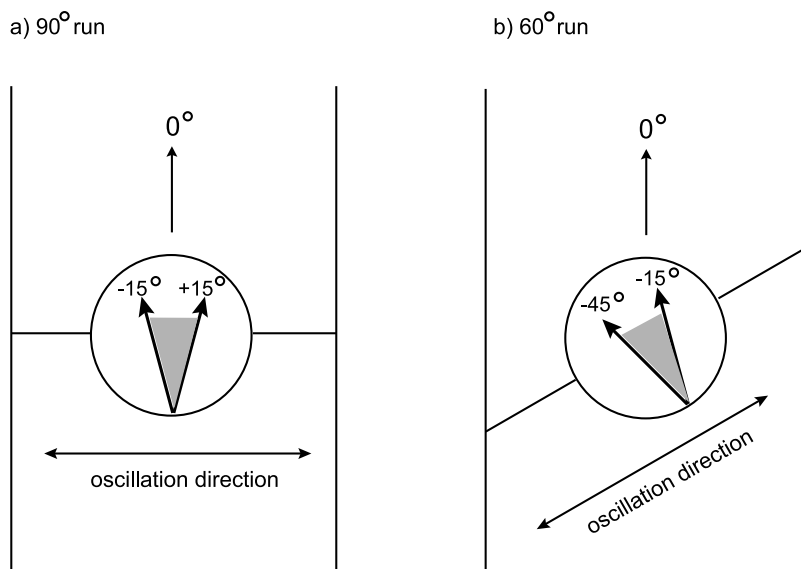


**Figure 2.** Sketch of reference orientation for ripple crests, plate configuration, and range of crest orientations included in calculation of mean wave-ripple  $\lambda$  for (a)  $90^\circ$  and (b)  $60^\circ$  runs.

a rectilinear grid with 4 mm spacing. Fourier decomposition was applied to an 80 cm  $\times$  80 cm region of the image in the central downstream portion of the plate, producing a two-dimensional spectrum of backscatter as a function of  $x$  and  $y$  frequencies ( $\text{m}^{-1}$ ). Each pair of  $x$  and  $y$  frequencies corresponds to a wavelength ( $\lambda = 1/\sqrt{f_x^2 + f_y^2}$ ) and orientation ( $\alpha = \arctan(-f_x/f_y)$ ). We define ripple orientation as the direction parallel to the crest over the range  $-90$  to  $90^\circ$ , where  $0^\circ$  is aligned with the downstream direction in the flume (Figure 2).

[11] On the basis of inspection of the distribution of amplitudes of the Fourier components of several scans from different runs an amplitude of 1 volt was identified as a threshold between signal and noise, and components with amplitudes below this threshold were discarded before calculating means or distributions of  $\lambda$  or  $\alpha$ . Mean wavelength was calculated as the amplitude-weighted average of the wavelengths from the remaining components. In addition, the amplitude-weighted mean wavelength was calculated from the subset of components with orientations within  $\pm 15^\circ$  of perpendicular to the plate motion (Figure 2). This quantity, which we call “mean wave-ripple  $\lambda$ ,” is used in sections 3.5 and 4.3.

[12] Wavelength derived from the sonar images is compared to physical measurements of the final beds in Figure 3. The root mean square (RMS) difference between the sonar mean and physical measurements was 2.4 cm based on the mean  $\lambda$  for 11 runs, and 1.9 cm based on the mean wave-ripple  $\lambda$  for eight runs with bed forms classified as linear or irregular ripples. Note that the RMS differences reflect sampling bias in the physical measurements as well as error in the sonar-derived values.

[13] The distribution of crest orientations  $\alpha$  derived from each sonar is biased by the beam direction, because the sonar predominantly detects features perpendicular to the beam. To minimize this bias, we averaged data from the two sonars. In the region of the bed analyzed for  $\lambda$  and  $\alpha$  the two

sonar beams were directed toward each other, crossing at angles ranging from approximately  $160^\circ$  to  $80^\circ$ . The backscatter data were averaged in frequency space rather than physical space, because the FFT regions for the two sonars (chosen to avoid the blanking region around each sonar) were not identical.

[14] To determine  $\alpha$  at the end of each run, amplitudes of the Fourier components from the last three image pairs from the two sonars were averaged. Then the three sonar-averaged amplitudes were averaged to reduce noise, assuming that ripples did not change significantly during the interval of the three scan-pairs (approximately 2.25 min). These averaged amplitudes were used to calculate circular variance and to investigate the distribution of  $\alpha$ . For the

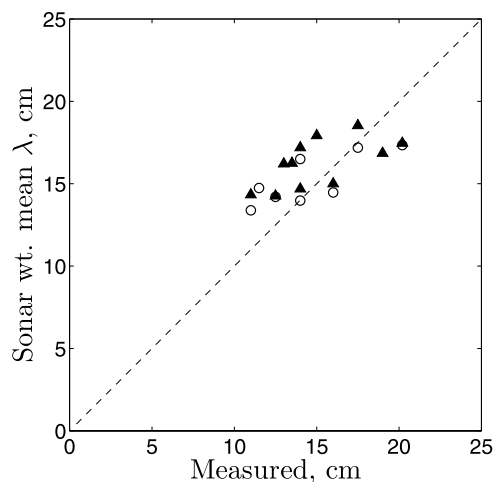


**Figure 3.** Mean ripple wavelength  $\lambda$  from sonar images versus average of physical measurements for weighted mean of all detected orientations (triangles) and weighted mean wave-ripple  $\lambda$  (see text) for runs with bed forms classified as linear or irregular wave ripples (circles).

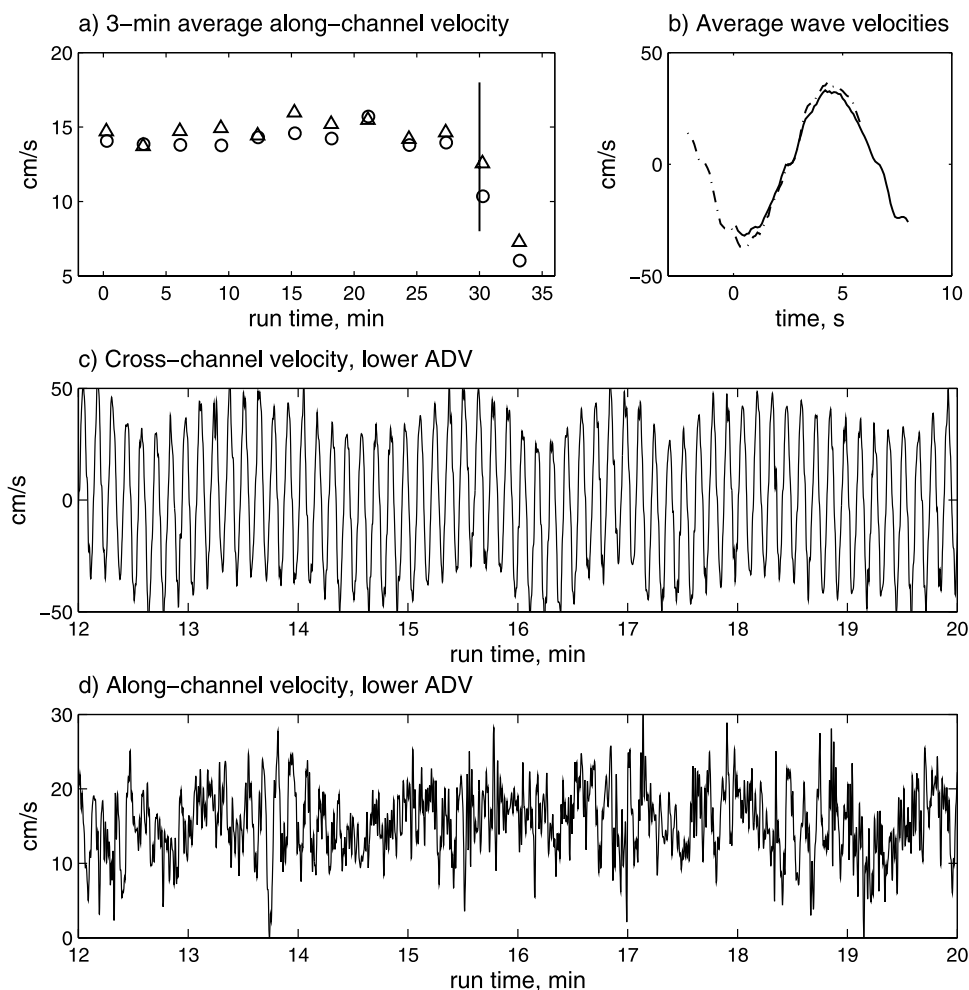


**Figure 4.** Current and wave velocities during run 14. (a) Three-minute average along-channel velocity measured by upper (circles) and lower (triangles) ADVs. Vertical line indicates the time that plate oscillations ended. (b) Phase-averaged cross-channel velocities from 110 waves measured by upper (solid line) and lower (dash-dotted lines) ADVs. (c) Cross-channel velocity measured by lower ADV during 8 min of run. (d) Along-channel velocity measured by lower ADV during 8 min of run. Velocities in Figures 4c and 4d have been low-pass filtered to remove frequencies greater than 1 Hz.

averaged amplitudes a noise threshold of 0.8 rather than 1 V was used.

### 3. Results

#### 3.1. Hydrodynamic Conditions

[15] Conditions for all runs are summarized in Table 1. Both nominal and measured values for depth-averaged current and wave orbital diameter are reported. The nominal depth-averaged current speed  $\bar{u}_n$  is based on the discharge rate and water depth in the flume, and the nominal oscillation excursion  $d_{on}$  and period  $T$  are those specified in the program controlling the motor.  $T$  was 8 s in all but one run (with  $T = 12$  s). The angle between plate motions and current was  $90^\circ$  in most runs, with three runs at  $60^\circ$  and two runs at  $45^\circ$ .

[16] Measured values were calculated from the ADV data collected 6 cm above the bed (cmab), and differed somewhat from the nominal values (Figure 4). Mean along-channel velocities were typically 15–20% higher than

nominal, and velocities 6 cmab were at times higher than at 16 cmab, likely owing to near-bed acceleration over the plate and sand bed (Figure 4a). Instantaneous cross-channel velocities show a pulsing in the oscillatory velocities: the difference between maximum and minimum velocity for each oscillation is consistent and close to the expected value, but they are offset at times by up to  $\pm 15$  cm/s, so that maximum speed exceeds expected values on one phase or the other of most oscillations (Figure 4c). Thus although the magnitude of averaged wave velocities (Figure 4b) was close to expected (on the basis of  $d_{on}$  and  $T$ ), the RMS wave velocity, which is more relevant to sediment transport, was greater than expected. In addition, a short delay at times of plate reversal (at  $u_w = 0$ ) produced a deviation from expected sinusoidal velocities (Figure 4b). Oscillation period was consistent with the nominal value, and wave velocities from the two ADVs were indistinguishable. There were fluctuations at the frequency of the plate oscillation in the instantaneous along-channel velocities (Figure 4d), and longer-period pulsing of the flow occurred as well. These

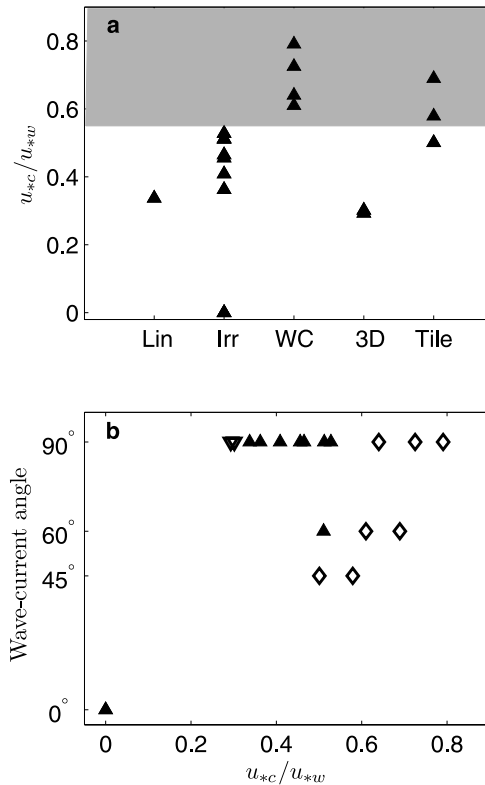


**Figure 5.** (a) Bed form category as a function of the ratio  $u_{*c}/u_{*w}$  of current friction velocity to maximum friction velocity due to waves. Shading indicates conditions dominated by three-dimensional (WC or T) bed forms ( $u_{*c}/u_{*w} > 0.55$ ). (b) Bed form type as a function of  $u_{*c}/u_{*w}$  and wave-current angle: Linear or irregular wave ripples (solid triangles), wave-current ripples or tiled bed forms (diamonds), 3D irregular bed forms (open triangles).

variations in the mean flow are likely produced by the interaction of the oscillating plate, sand bed, and instrumented frame with the current.

[17] Measured  $u_b$ ,  $d_o$ , and  $\bar{u}$  are calculated as follows. The average along-flume velocity is extrapolated to a depth-averaged value  $\bar{u}$  based on the measured height of the ADV sampling volume, assuming a logarithmic profile. Wave orbital velocity  $u_b$  is  $\sqrt{2}u_{wRMS}$ , where  $u_w$  is the component of oscillatory velocity along the axis of plate motion. The orbital diameter  $d_o$  is  $u_b T/\pi$ .

[18] Four nondimensional numbers are listed in Table 1 to characterize hydrodynamic conditions. The Keulegan Carpenter number  $KC = u_b T/D$  represents the ratio of the drag force to the pressure gradient force on a body under a wave [Sleath, 1984]. In our experiments the minimum  $KC$  exceeded 6400, indicating that drag is the dominant force on sediment particles, so that the increased role of inertia in sediment transport for an oscillating plate, compared to surface waves, is not significant in these experiments.

### 3.2. Bed Form Categories

[19] Bed forms observed at the end of each run were classified into one of six types: linear wave ripples, irregular wave ripples, wave-current ripples, tiled bed forms, 3D irregular bed forms, or current bed forms. Linear and

irregular wave ripples are characterized by crests predominantly perpendicular to the direction of plate oscillation. Linear wave ripples (LR) have several crests that are continuous over the entire length of the plate, whereas irregular wave ripples (IR) have more bifurcations. Wave-current ripples (WC) have two sets of crests with different orientations: one approximately perpendicular to the oscillation and the other approximately perpendicular to the current. Tiled bed forms (T) have crests with more than two orientations that form closed polygons (typically hexagons). Bed forms classified as 3D irregular (3D) have short discontinuous crests with many orientations and a wide range of bed form heights. The largest bed forms we observed are in this category. Current bed forms (C) have one set of crests which are perpendicular to the mean flow direction. The only final bed classified as current bed forms was that of run 8, which consisted of a single current dune.

[20] To investigate the dependence of bed form type on wave and current forcing, maximum friction velocity due to waves  $u_{*w}$  and due to current  $u_{*c}$  were estimated using the Grant-Madsen wave-current boundary layer model (GM) [Grant and Madsen, 1979; Madsen, 1994]. In GM we used  $u_b$  from Table 1 for bottom orbital velocity. We used bottom roughness  $k_b = 1$  cm, to represent an average bed form height during the runs, because bed forms have been shown to increase roughness (and near-bed turbulence) significantly compared to grain roughness [Nielsen, 1992]. Differences in bed form height between the runs were not taken into account because of the uncertainty in predicting hydrodynamic roughness from bed form dimensions and the changing ripple dimensions over the course of the runs.

[21] Li and Amos [1998] found that “pure” wave ripples occur when  $u_{*c}/u_{*w} < 0.5$ , and combined wave-current ripples occur for  $0.5 < u_{*c}/u_{*w} < 0.8$ , on the basis of field data. In our data ratios of  $u_{*c}/u_{*w} > 0.55$  produced three-dimensional bed forms (categories WC or T) (Figure 5a). Wave ripples (LR or IR) occurred for  $u_{*c}/u_{*w} < 0.55$ , but some three-dimensional bed forms were produced in this range as well. Both cases of 3D irregular bed forms occurred at relatively low ratios of  $u_{*c}/u_{*w}$ . The influence of current on bed forms appears to increase as wave-current angle decreases. The tiled bed with  $u_{*c}/u_{*w} = 0.5$  was produced by a  $45^\circ$  run. Similar values of  $u_{*c}/u_{*w}$  produced wave ripples at wave-current angles of  $90^\circ$  and  $60^\circ$  (Figure 5b). Photographs show that the wave ripples were more irregular at  $60^\circ$  than at  $90^\circ$ .

[22] The occurrence of the 3D irregular bed forms in runs with relatively low currents and large oscillations indicates that factors other than relative current strength can produce 3D bed forms. In experiments with regular waves (and no current) in a water tunnel, O’Donoghue and Clubb [2001] observed that 3D bed forms frequently formed as a transitory stage during the growth of 2D vortex ripples. They also observed that 2D ripples never developed in experiments with fine grains ( $D < 0.26$  mm) and low mobility number  $\psi$  ( $\psi = u_b^2/[(s-1)gD]$  where  $u_b$  is bottom orbital velocity,  $g$  is gravitational acceleration, and  $s$  is the relative density of sediment); instead, small nonstatic 3D bed forms persisted. Their description is not consistent with the 3D bed forms observed in our study, which were large and occurred for  $D = 0.27$  mm and  $\psi > 30$ . The 3D bed forms were not

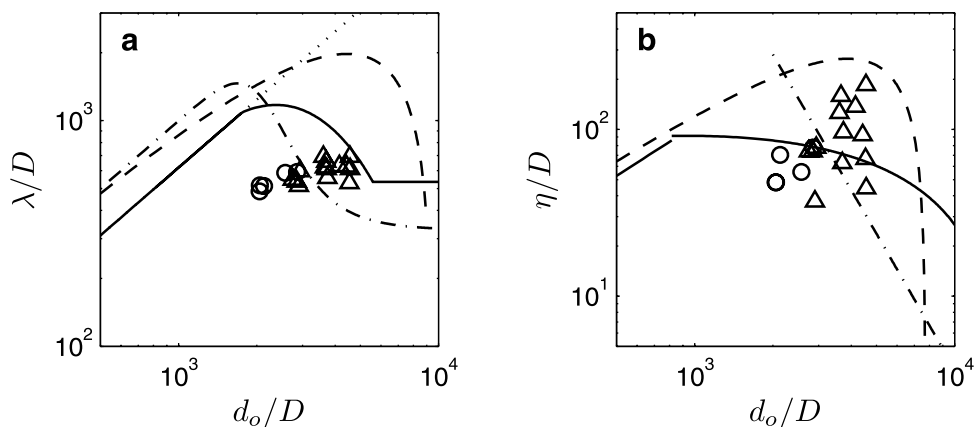


**Figure 6.** Predicted and measured ripple wavelength (a) and height (b) vs. wave orbital diameter, with both axes normalized by grain size. Triangles represent  $90^\circ$  runs, circles are  $60^\circ$  or  $45^\circ$  runs. The predictions are Wiberg-Harris (solid line), and (with  $T = 8$  s) Nielsen-field (dash-dotted line), Nielsen-lab (dashed line).

transitory: the bed became increasingly three-dimensional during the run.

### 3.3. Ripple Dimensions

[23] Wave ripples can be categorized on the basis of the ratio  $d_o/D$  of wave orbital diameter to median grain diameter [Clifton and Dingler, 1984; Wiberg and Harris, 1994]. Orbital ripples, for which both wavelength and height depend directly on  $d_o$ , and steepness is constant, occur for  $d_o/D$  less than about 2000. Anorbital ripples are characterized by wavelength that is a function of grain size and is independent of  $d_o$ , and ripple height that decreases with increasing  $d_o$ , and occur for  $d_o/D > 5000$ . For  $2000 < d_o/D < 5000$  the relationship between ripple wavelength, height, steepness and  $d_o/D$  is less clear; ripples in this transition region are known as suborbital ripples. A number of researchers have quantified these relationships and developed empirical formulae for predicting wavelength and height of wave ripples as a function of  $d_o/D$  [Wiberg and Harris, 1994], or of  $d_o$ ,  $D$ , and wave period  $T$  [Nielsen, 1981; Grant and Madsen, 1982; Mogridge et al., 1994;

Styles and Glenn, 2002; Faraci and Foti, 2002; Grasmeijer and Kleinhans, 2004; Williams et al., 2005]. The predictions tend to differ most for suborbital ripples.

[24] Wavelength  $\lambda$  and height  $\eta$  of the ripples produced in our experiments are compared to three empirical predictors in Figure 6, to examine how these combined flow results differ from predictions developed for wave ripples. The empirical predictors are Wiberg and Harris [1994], and the field and laboratory equations proposed by Nielsen [1981]. In Figure 6,  $\lambda$  is the average of the weighted mean wavelength from the last three pairs of sonar images of each run,  $\eta$  is the average of the measured ripple heights (typically 5 measurements), and  $d_o$  is calculated from the ADV data (Table 1). The  $d_o/D$  ratios in our runs are expected to produce orbital and suborbital ripples. Ripple wavelengths are consistently lower than predicted by the Wiberg-Harris or Nielsen-laboratory equations.  $\lambda/D$  as a function of  $d_o/D$  in our experiments are within the range of other full-scale oscillatory laboratory studies [O'Donoghue et al., 2006], and of the small wave-generated ripples summarized by Williams et al. [2005], although below the

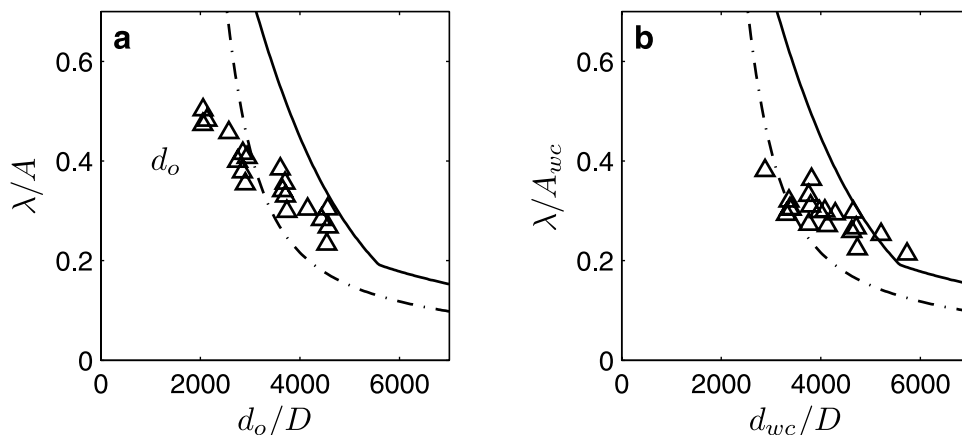


**Figure 7.** (a) Ripple wavelength/wave semiexcursion versus wave orbital diameter/grain size, (b) ripple wavelength/wave-current semi-excursion versus wave-current orbital diameter/grain size. The predictions are Wiberg-Harris (solid line) and Nielsen-field with  $T = 8$  s (dashed line).

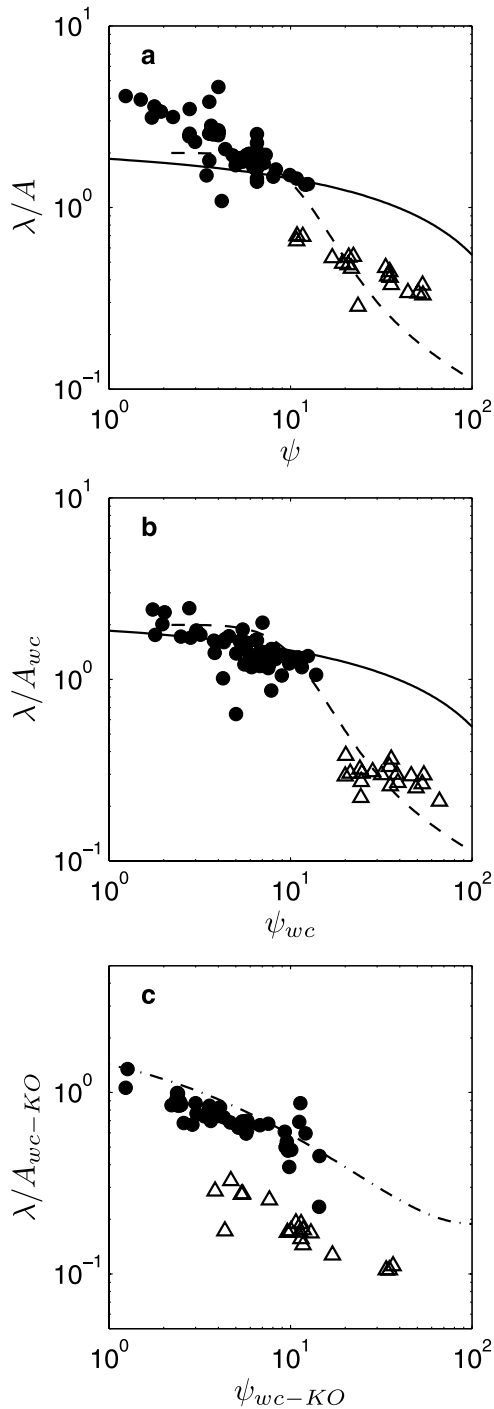


**Figure 8.** Ripple wavelength normalized by wave semi-orbital excursion  $\lambda/A$  versus mobility number  $\psi$ . (a)  $A$  and  $\psi$  for waves alone, (b) wave-current  $A$  and  $\psi$ , and (c) wave-current  $A$  and  $\psi$  according to KO equations, for KO data (circles) and our data (triangles). The predictions are Nielsen-lab (solid line), Nielsen-field (dashed line), KO (dash-dotted line).

average  $\lambda/D$ . All our observed  $\lambda$  are greater than the maximum ripple spacing from oscillating bed experiments of 10 cm for  $D = 0.3$  mm reported by *Miller and Komar* [1980].

[25] Steepness  $\eta/\lambda$  ranged from 0.07 to 0.27, with a mean of 0.15 (number of runs  $N = 17$ ). For bed forms classified as linear or irregular wave ripples, values were typical of orbital vortex ripples ( $0.14 < \eta/\lambda < 0.19$ , mean 0.16,  $N = 8$ ). Rolling-grain ripples, which have been produced in some oscillating bed experiments, have a maximum steepness of 0.1 [*Miller and Komar*, 1980]. The tiled and wave-current bed forms had slightly lower  $\eta/\lambda$  than the wave ripples, with an average of 0.11.

[26] Figure 6 shows that the range of  $\lambda$  and  $\eta$  for each  $d_o/D$  is at least as great as the differences between the means. To what extent does current strength account for this variation? Current can influence ripple evolution in at least two ways: by increasing fluid excursion (and maximum velocity) during the wave period and by increasing the relative importance of suspended sediment to bedload transport. *Wiberg and Harris* [1994] hypothesize that orbital ripples are formed predominantly by bedload transport and are characterized by  $\eta$  greater than the thickness of the wave boundary layer. Increased current may erode ripple crests and increase suspended sediment transport, producing suborbital or anorbital, rather than orbital, ripples.

[27] To account for increased excursion, *Khelifa and Ouellet* [2000] (KO) proposed that wave-current flows be characterized by the effective fluid orbital diameter  $d_{wc}$ , rather than  $d_o$ . We calculated  $d_{wc}$  as the vector sum of the excursion due to current near the bed  $u_\delta$  during one-half wave period and  $d_o$ :

$$d_{wc} = \left[ d_o^2 + \left( \frac{T}{2} u_\delta \right)^2 + T d_o u_\delta \cos \beta \right]^{0.5} \quad (1)$$

where  $\beta$  is the angle between waves and current. This definition for  $d_{wc}$  differs from the expression in KO in using  $u_\delta$  rather than  $\bar{u}$  and scaling the current component by  $T/2$  rather than  $T$ . For these experiments, where the water depth was 0.5 m, we used  $u_\delta = 0.65 \bar{u}$ , an estimate of the current velocity at 2 cm above the bed, assuming a logarithmic velocity profile, bed roughness  $k_b = 1$  cm, and  $z_0 = k_b/30$ .

[28] Normalizing  $\lambda$  by  $A_{wc} = d_{wc}/2$  rather than  $A = d_o/2$  reduces the RMS difference between predicted and measured normalized  $\lambda$  from 0.31 to 0.08 for the Nielsen-field predictive relationship and from 0.53 to 0.36 for the Wiberg-Harris predictive relationship for  $\lambda/A$  as a function of  $d_o/D$  (Figure 7).

[29] The Nielsen relationships predict  $\lambda/A$  as a function of mobility number  $\psi$ , a nondimensional ratio of the mobilizing force of waves to the stabilizing force of gravity. To calculate a wave-current mobility number  $\psi_{wc} = u_{wc}^2 / [(s-1)gD]$ , we estimate the maximum velocity near the bed during the wave period as

$$u_{wc} = [u_b^2 + u_\delta^2 + 2u_\delta u_b \cos \beta]^{0.5} \quad (2)$$

[30] When the contribution of current to mobility number is ignored, the KO experiments produced greater  $\lambda/A$ , whereas our experiments produced smaller  $\lambda/A$ , than predicted (Figure 8a). Substitution of  $A_{wc}$  for  $A$  and  $\psi_{wc}$  for  $\psi$  improves agreement with Nielsen's predictive equations for

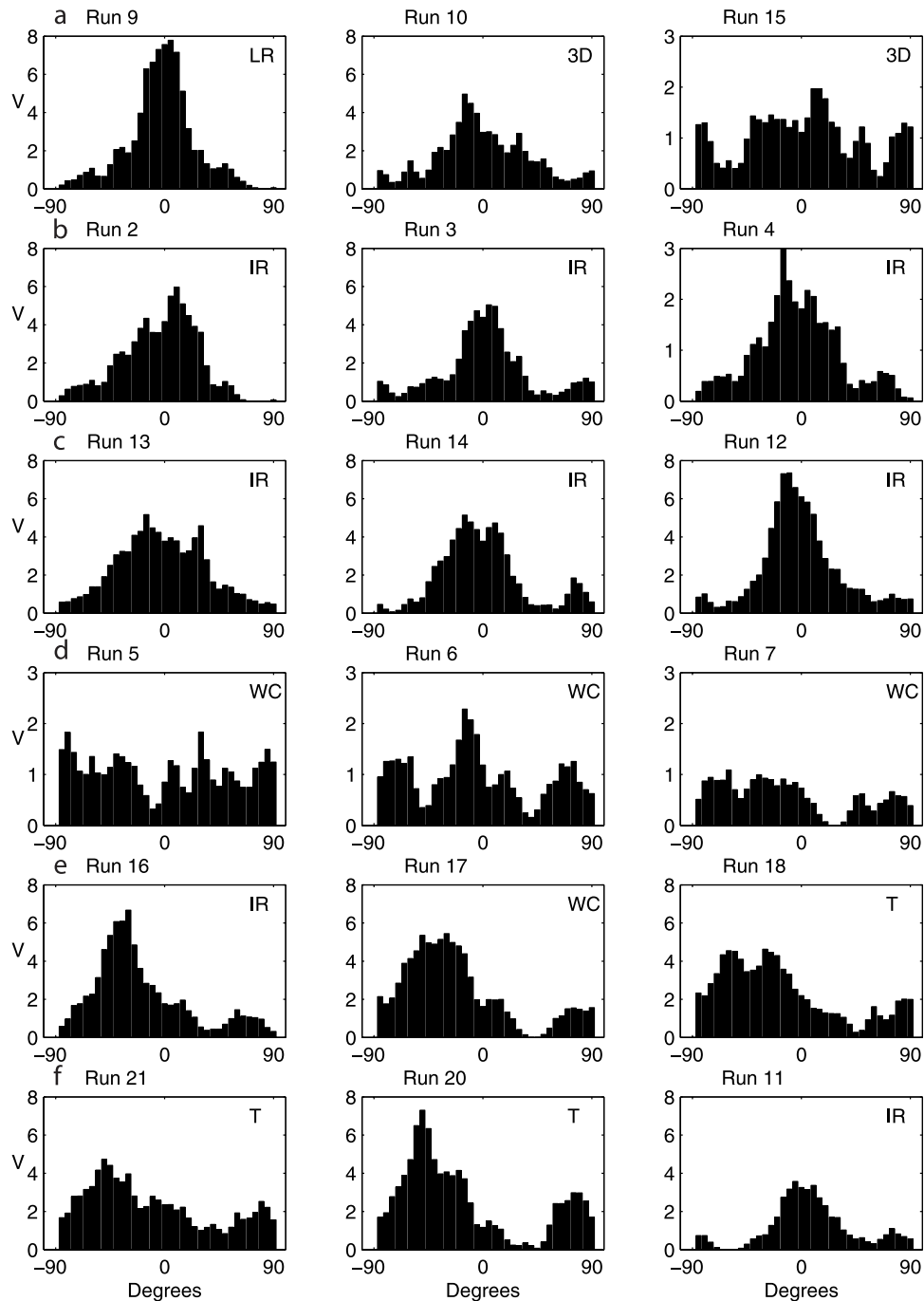


**Figure 9.** Distributions of ripple crest orientations at the end of the run by average amplitude of backscatter in volts (V), derived from sonar images. (a)  $\bar{u} = 6$  cm/s; (b, c)  $\bar{u} = 12$  cm/s; (d)  $\bar{u} = 23$  cm/s; (e)  $\beta = 60^\circ$ ; (f)  $\beta = 45^\circ$  except right plot for which  $\bar{u} = 0$ . In each row  $u_{*w}/u_{*c}$  increases from the left plot to the right. Note smaller scale on y-axis in the plots for runs 15, 4, and 5–7: In these runs signal strength was weaker because of high suspended-sediment concentrations.

both our data (RMS difference between measured and predicted values reduced from 0.31 to 0.11) and that of KO (RMS difference reduced from 1.08 to 0.35) (Figure 8b). The KO data were compared to Nielsen's laboratory equation because of the low range of  $\psi$ . For our data, Nielsen's field equation is a better predictor than the laboratory equation. In contrast, a number of other full-scale laboratory experiments have produced ripple wavelengths closer to the

Nielsen-laboratory than to the Nielsen-field predictions [*O'Donoghue et al.*, 2006], although the scatter of results in the suborbital range is great.

[31] Accounting for current brings both the KO and our data sets closer to the predicted values because they have different ranges of  $d_o/D$ . In the KO experiments maximum  $d_o/D$  is approximately 400, corresponding to the lower part of the orbital ripple range, for which  $\lambda$  increases with

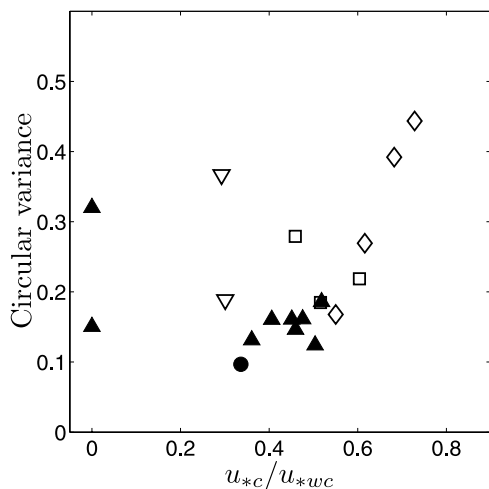


**Figure 10.** Circular variance versus  $u_{*c}/u_{*wc}$  for the bed form categories LR (solid circle), IR (solid triangles), WC (open diamonds), T (open squares), and 3D (open triangles).

excursion (Figure 6). In our experiments, increasing excursion moves  $d_o/D$  further into the suborbital range ( $d_o/D > 2000$ ), and decreases expected  $\lambda$ .

[32] The contribution of current to fluid excursion does not account for all of the differences between the pure waves and combined flows, or between the bed forms produced by the two types of flows. As a result we do not expect the Nielsen or Wiberg-Harris equations to be accurate predictors of  $\lambda$  for combined flows, even when  $\psi_{wc}$  or  $d_{wc}$  is used. Combined flows produce three-dimensional as well as two-dimensional bed forms, and the presence of current may increase the ratio of suspended to bedload transport. These factors may explain the difference between our data and Nielsen's relationship in the slope of  $\lambda/A_{wc}$  versus  $\psi_{wc}$ . Our results indicate that including the current contribution is necessary but not sufficient for predicting wavelengths for combined-flow bed forms. Modifying existing predictive relationships to account for current is a reasonable approach to estimating ripple dimensions until adequate data are available to support the development of predictive relationships specific to combined flows.

[33] Khelifa and Oullet proposed a relationship between  $\lambda/A_{wc-KO}$  and  $\psi_{wc-KO}$  based on their data, where  $u_{wc-KO}$  is calculated as  $d_{wc-KO}/T$ . Our data do not fit the KO relationship, and the KO scaling for  $\psi_{wc-KO}$  does not distinguish between the two data sets (Figure 8c), despite the higher range of  $u_b$  in our experiments (and comparable current speeds). Note that  $u_{wc-KO}$  corresponds to an average rather than a maximum velocity over the wave period, and does not reduce to  $u_b$  for  $\bar{u} = 0$ .

### 3.4. Bed Form Orientation

[34] To extract the dominant orientation of crests from the sonar images, we first identified the number of modes in the distribution of orientations and then determined a representative orientation for each peak. Histograms with  $5^\circ$  bins of crest orientation  $\alpha$  weighted by amplitude of the Fourier component were created from the averaged amplitudes (calculated as described in section 2.2) and smoothed using a moving average of five adjacent points with weighting (1,

3, 5, 3, 1) (Figure 9). Note that crest orientation is defined over the range  $\pm 90^\circ$  ( $90^\circ$  and  $-90^\circ$  are parallel). The number of peaks in each distribution and the range of angles associated with the peak were determined from the smoothed histograms. Three runs have three peaks (runs 6, 7, and 19), seven have two peaks (runs 3, 11, 14, 15, 16, 18, 20), and the rest are unimodal. Two representative orientations were extracted for each peak: the apex of the peak in the smoothed histogram and the amplitude-weighted mean orientation over the range of angles associated with each peak. We call the weighted mean a dominant orientation.

[35] The spread of the  $\alpha$  distributions was characterized by calculating the circular variance  $S_0$  for a  $180^\circ$  range, where  $0 < S_0 < 1$  [Mardia, 1972].  $S_0$  increases with  $u_{*c}/u_{*wc}$  (Figure 10). Average circular variance is greater for 3D (open symbols in Figure 10) than 2D bed forms, although there is no clear threshold in  $S_0$  between 2D and 3D beds.

[36] The number of peaks in the distributions of  $\alpha$  from the sonars does not always agree with the number of crest orientations detected by eye. In some cases the sonar distributions show a single broad peak where we observed two or three crest orientations. For example, in run 21

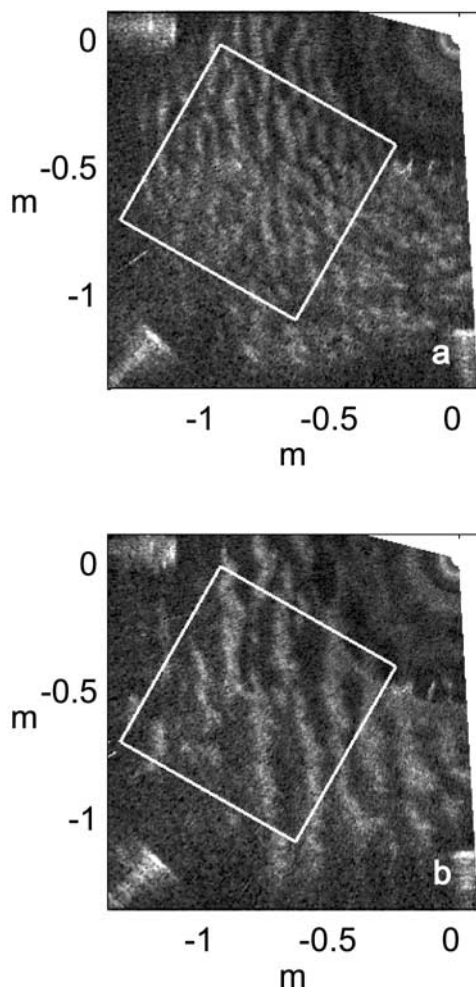


**Figure 11.** Sonar images (a) 7.5 min and (b) 42.5 min into Run 9. White box shows region used for 2D FFT. The three bright spots are legs of instrument frame. Sonar is mounted on leg in upper right of frame.

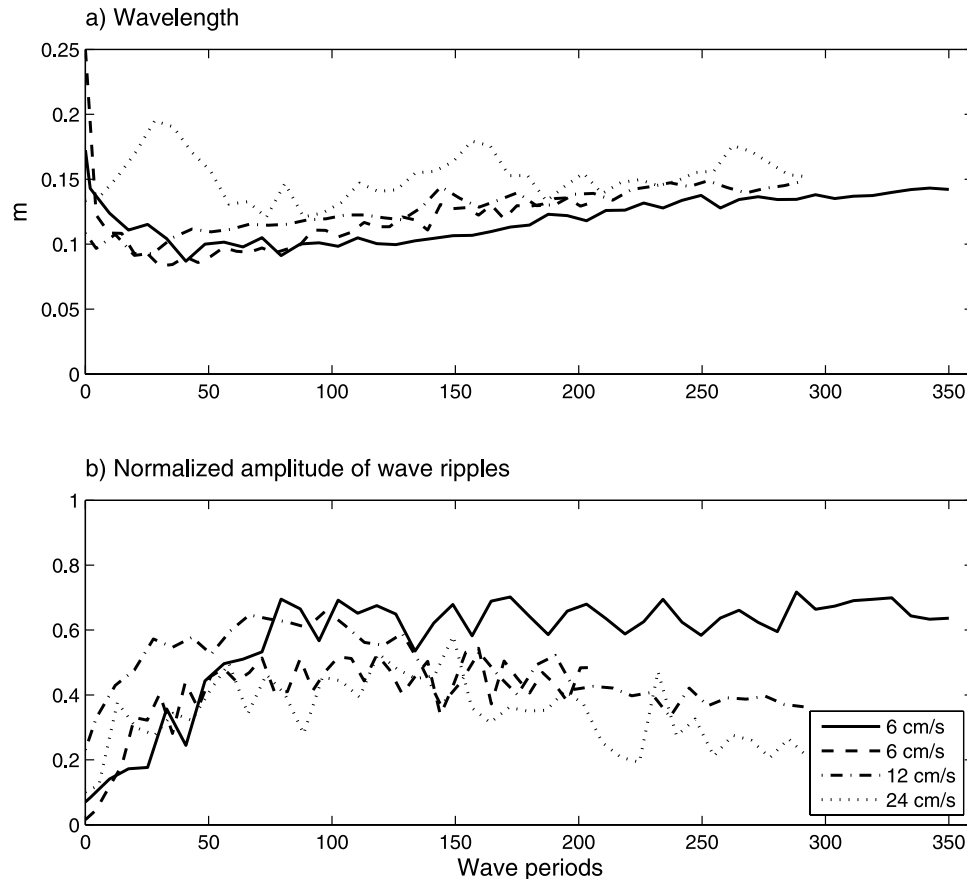


**Figure 12.** Evolution as a function of number of wave periods of (a) mean wave-ripple  $\lambda$  and (b) amplitude of components comprising wave ripples as a fraction of sum of all amplitudes at the end of the run, for four runs with wave mobility number  $\psi$  between 17 and 26.

(Figure 9f, and Figure 15c in section 4.1) we observed trends of  $-45^\circ$  (dominant),  $45^\circ$ ,  $0^\circ$ , and  $80^\circ$ . While minor peaks close to all of these orientations except  $45^\circ$  can be detected in the sonar distribution, only one ( $-45^\circ$ ) met our definition of “peak.” In cases such as these, the three-dimensionality of the bed forms can be identified from the sonar results by the high circular variance although only one peak is identified. The discrepancy between peaks detected by the human eye and by the sonars may be due to poor resolution by the sonars, or to a human tendency to emphasize topographic features that are laterally extensive even where relief is low. We believe that the sonar-derived distributions are a more objective method for assessing crest orientations than visual observation, but formal testing of their accuracy awaits further data.

### 3.5. Bed Form Evolution

[37] Inspection of sequences of sonar images from several runs producing linear or irregular wave ripples shows that ripple wavelength evolution was consistent with the observations of *Doucette and O’Donoghue* [2006] and *Hansen et al.* [2001]. The first ripples to appear are small and two-dimensional, with typical wavelengths of 8–10 cm in our experiments (Figure 11a). After an initial period of growth some of the crests merge, reducing the number of crests and introducing crest bifurcations that increase the three-dimensionality of the bed. The remaining crests become

more two-dimensional (Figure 11b) and gradually spread apart (slide) until equilibrium wavelength is attained. (The words “merge” and “slide” are the terminology of *Doucette and O’Donoghue* [2006].) In runs culminating in three-dimensional bed form categories (WC, T, or 3D), the first bed forms to appear were typically two-dimensional, and the beds became increasingly three-dimensional as the runs progressed.

[38] Time series of mean wave-ripple  $\lambda$  for  $90^\circ$  runs are shown in Figure 12 for  $17 < \psi < 26$  ( $d_{on} = 60$  cm and run 12), and in Figure 13 for  $33 < \psi < 36$  ( $d_{on} = 80$  cm). Figures 12b and 13b show the sum of the amplitudes of the Fourier components comprising the mean wave-ripple  $\lambda$  normalized by the sum of all amplitudes at the end of the run. This quantity increases as wave ripple height grows, and decreases as three-dimensionality (i.e., growth of ripples not perpendicular to oscillations) increases.

[39] For the smaller waves (Figure 12), coherent wave ripples are not visible in the sonar images until 40–60 wave periods into each run (note low values of normalized amplitudes in Figure 12b).  $\lambda$  evolved most slowly for the two runs with lowest current speed: equilibrium wavelength may not have been reached at the end of the run, although the rate of growth had decreased. In runs with  $d_{on} = 80$  cm, detectable ripples formed more quickly than for the less energetic waves, and almost immediately began to grow

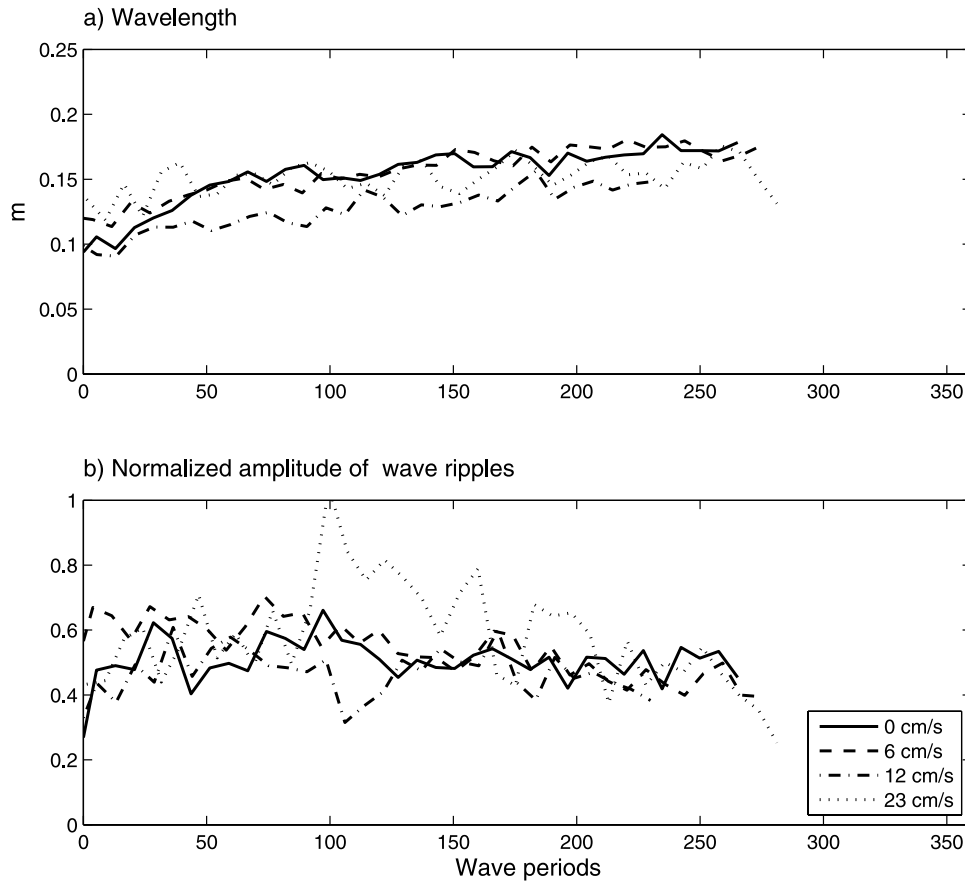


**Figure 13.** Evolution as a function of number of wave periods of (a) mean wave-ripple  $\lambda$  and (b) amplitude of components comprising wave ripples as a fraction of sum of all amplitudes at the end of the run, for four runs with wave mobility number  $\psi$  between 33 and 36 ( $d_{on} = 80$  cm).

rapidly. Ripple wavelength stabilized after about 200 wave periods.

[40] Runs 2, 3, and 4 were started from the bed left by the previous run, rather than from a flat bed. These runs provide an estimate of the number of wave periods required for a rippled bed to respond to a change in wave conditions. Mean wave ripple  $\lambda$  increased as  $d_{on}$  increased from 60 to 80 cm, but decreased after  $d_{on}$  increased to 100 cm (Figure 14), suggesting that conditions had crossed a

threshold from producing orbital to producing suborbital ripples. Current speed was constant in these runs.

#### 4. Discussion

##### 4.1. Review of Wave-Current Velocities and Transport

[41] The direction of instantaneous velocity in a combined flow is determined by the time-varying vector sum of the wave velocity and the current. This direction varies vertically, because the current boundary layer is much

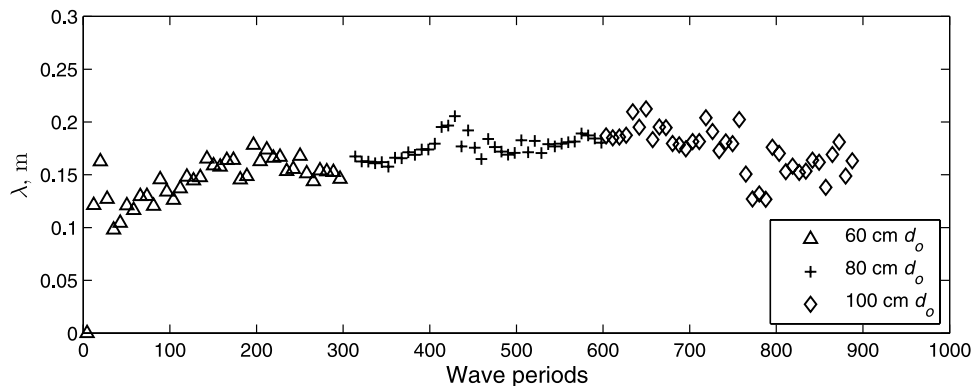


**Figure 14.** Evolution of mean wave-ripple  $\lambda$  for Runs 2, 3, and 4, as a function of number of wave periods. Current speed is 14 cm/s.

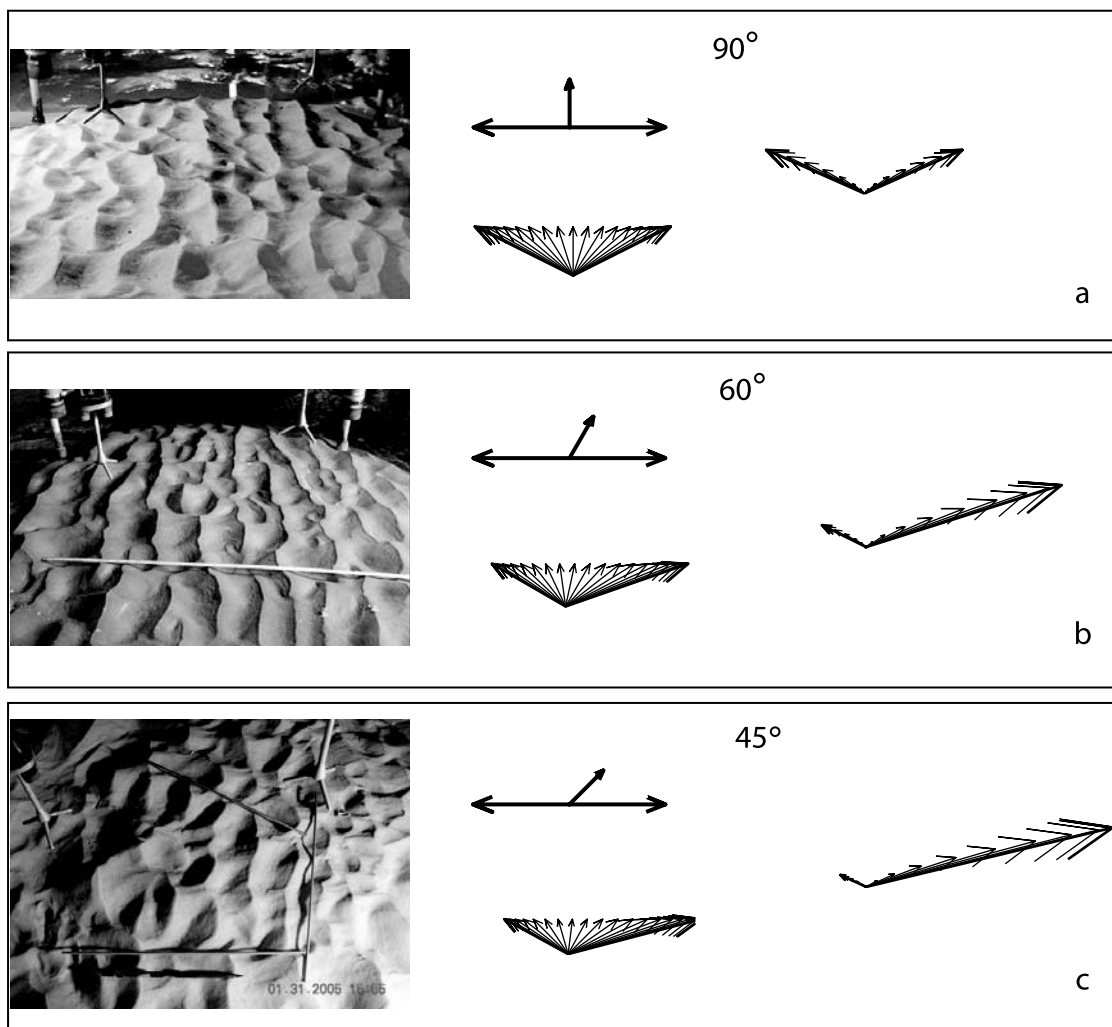


**Figure 15.** Schematic of the influence of current and wave-current angle on instantaneous velocity and transport. Final beds, wave and current directions (top of each middle plot), instantaneous velocity vectors (bottom of each middle plot), and estimated instantaneous transport (right plots) for three runs with  $\bar{u} = 12$  cm/s and  $u_b = 24$  cm/s, and wave-current angles of (a)  $90^\circ$  (run 13), (b)  $60^\circ$  (run 16), and (c)  $45^\circ$  (run 21). Vectors are calculated from nominal run parameters.

thicker than the wave boundary layer. The middle column (lower images) of Figure 15 illustrates the theoretical direction of the instantaneous velocity at equal time steps, based on the nominal depth-averaged velocity, oscillation amplitude, and wave-current angle  $\beta$  for three runs. For  $\beta = 90^\circ$  the instantaneous velocity vectors during the two phases of the wave are symmetric about the direction of the current, and maximum speed occurs twice during the wave period. For  $\beta < 90^\circ$  maximum speed occurs once per period, during the phase that is more closely aligned with the current direction.

[42] The directional distribution of instantaneous sediment transport is more concentrated than that of velocity, because transport scales with velocity cubed (Figure 15, right). For Figure 15, bed shear stress  $\tau_b$  and friction velocity due to waves and currents were calculated using GM with a bed roughness  $k_b = 1$  cm, and transport was calculated from  $\tau_b$  using the formulation of Meyer-Peter

and Muller [1948] (see section 4.2.1). The majority of transport is in the direction of the combined  $\tau_b$  at the time of maximum speed, for the wave and current conditions in Figure 15. For  $\beta = 90^\circ$  maximum transport during the two phases of the wave is symmetric about the direction of the current, so that the phase-averaged transport is downstream. For  $\beta < 90^\circ$ , net transport is directed between the directions of maximum transport and the current. The maximum instantaneous  $\tau_b$  increases as the wave-current angle decreases, for constant  $\bar{u}$  and  $u_b$  (as in Figure 15). Bed forms produced by unidirectional flows are typically more three-dimensional than those produced by waves [Dumas *et al.*, 2005]. The same mechanism may account for the increasing three-dimensionality of bed forms as  $\beta$  decreases and transport is concentrated in a single direction.

#### 4.2. Bed Form Orientation

[43] The most obvious feature of the bed forms created by wave-current angles of  $45^\circ$  and  $60^\circ$  is multiple sets of crests

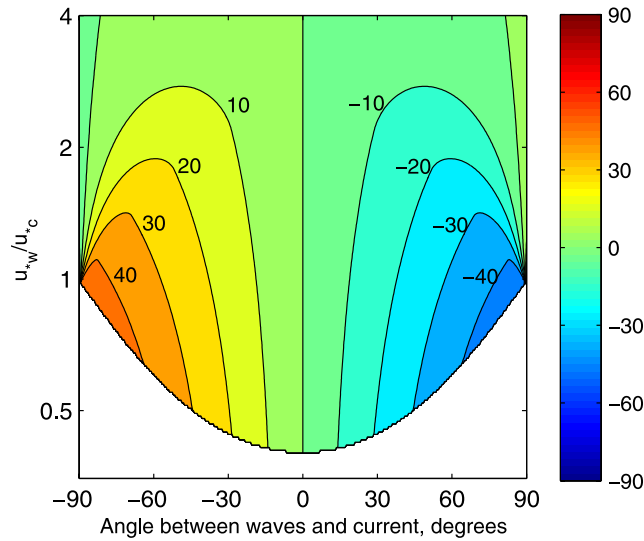


**Figure 16.** Crest orientation maximizing GBNT: predicted rotation from perpendicular to wave direction in degrees, clockwise positive. White indicates that bed sediment is not mobilized: shear stress is below the threshold for sediment motion throughout the wave period. Here  $u_{*c} = 1$  cm/s,  $D = 0.27$  mm.

with different orientations. Three of the five runs in this category produced tiled bed forms with three trends, and one produced wave-current bed forms with two trends (see section 3.2 and Figure 15c).

[44] Both waves and currents alone produce bed forms with crests oriented perpendicular to the direction of flow. The expected orientation of bed forms produced by combined wave-current flows is not intuitively obvious. We identified four factors that could potentially control bed form orientation: the directions of waves, current, maximum instantaneous bed shear stress  $\tau_b$ , and maximum gross bed form normal transport (GBNT). GBNT is the sum of the absolute value of transport normal to a bed form crest resulting from multiple transport directions.

[45] The concept of maximum gross bed form normal transport (MGBNT) was initially developed to account for bed form alignment in directionally varying steady flows [Rubin and Hunter, 1987; Rubin and Ikeda, 1990]. In combined wave-current flows, crests maximizing GBNT are perpendicular to waves for  $\beta = 90^\circ$ . For  $\beta < 90^\circ$ , the alignment of crests maximizing MGBNT is rotated from perpendicular to waves, with the amount and direction of rotation dependent on  $u_b$ ,  $\bar{u}$ , and  $\beta$  (see section 4.2.1). Gallagher et al. [1998] showed that the direction of mega-ripple migration in combined wave-current flows in the surf zone is consistent with the direction of MGBNT.

#### 4.2.1. Application of MGBNT to Combined Flows

[46] In directionally varying steady flows, the orientation of bed forms  $\alpha$  is determined by the combined influence of the transport directions over the timescale of bed form development: bed forms align to maximize GBNT. For two alternating flow directions,  $\alpha$  is normal to the vector sum of the two transport vectors when the angle between the two directions  $\gamma$  is less than  $90^\circ$ , but for  $\gamma > 90^\circ$  the bed

form alignment maximizing GBNT is normal to the vector sum of one transport vector and the negative of the second. Thus  $\gamma > 90^\circ$  produces longitudinal or oblique bed forms. This result was initially based on experiments in air [Rubin and Hunter, 1987] and water [Rubin and Ikeda, 1990], and has been reproduced in subsequent numerical simulations of bed form development [Werner, 1995; Nishimori et al., 1998; Kocurek and Ewing, 2005].

[47] Rubin and Hunter [1987] express the direction of MGBNT as a function of the ratio  $R$  of transport in the two directions and  $\gamma$ . For combinations of steady flows,  $R$  can be determined from the duration and speed of each flow direction. The relative transport due to waves and currents is more difficult to estimate. The boundary layer produced by oscillatory flows is not fully developed, so the ratio between depth-averaged velocity and bottom shear stress is not the same as for unidirectional flows. In addition, the wave and current boundary layers influence each other; in particular, the near-bed turbulence created by the waves enhances the current shear stress [Grant and Madsen, 1979]. Thus the total transport cannot be simply decomposed into a sum of wave-induced and current-induced transport.

[48] For combined wave-current flows, we predict the crest orientation that maximizes GBNT as follows (Figure 16). Instantaneous bed shear stress is estimated at intervals of  $T/20$  over the wave period  $T$  as  $\tau_t = \rho u_{*wc}$  where  $u_{*wc}$  is the vector sum of  $u_{*c}$  and  $u_{*w} \cos 2\pi t/T$ . To estimate instantaneous transport, we apply the Meyer-Peter and Muller [1948] equation for equilibrium bedload transport at each timestep:

$$\Phi_B = \begin{cases} 8(\theta_t - \theta_c)^{1.5} & \theta_t \geq \theta_c \\ 0 & \theta_t < \theta_c \end{cases} \quad (3)$$

where  $\theta_t = \tau_t/[\rho(s-1)gD]$  is the instantaneous Shields parameter, and the critical Shields parameter  $\theta_c = 0.04$  is the threshold for sediment motion. For each combination of  $u_{*w}/u_{*c}$  and  $\beta$ , the absolute value of the component of transport normal to crests is summed over a wave period for crest orientations ranging from  $-90^\circ$  to  $90^\circ$ , and  $\alpha$  maximizing GBNT is identified. This approach assumes that bedload transport dominates bed form evolution, and that wave velocity  $u_w$  is in phase with  $\tau_w$ , neglecting the phase lead of  $\tau_w$  relative to  $u_w$  that has been observed experimentally [Sleath, 1978]. To predict  $\alpha$  on the basis of MGBNT for the experimental runs,  $u_{*w}$  and  $u_{*c}$  are calculated with GM as described in section 3.2.

[49] Figure 16 presents the MGBNT predictions as a function of the ratio  $u_{*w}/u_{*c}$  of peak wave to current friction velocity and  $\beta$ . Because of the incorporation of the threshold for sediment motion  $\theta_c$ , the MGBNT predictions depend not only on  $u_{*w}/u_{*c}$  and  $\beta$ , but also on the absolute level of  $u_{*c}$  and grain size. Figure 16 assumes  $u_{*c} = 1$  cm/s and  $D = 0.27$  mm; for these values, which are typical of our runs, current shear stress alone is not sufficient to mobilize the sediment. The white region at the bottom of Figure 16 indicates conditions for which  $\theta_t < \theta_c$  throughout the wave period (i.e., no sediment motion). The predicted range of conditions for significant rotation of bed forms (from normal to wave direction) is relatively narrow:  $0.5 < u_{*w}/u_{*c} < 3$  for  $\beta = 20^\circ$  and  $0.75 < u_{*w}/u_{*c} < 2$  for  $\beta = 75^\circ$ .

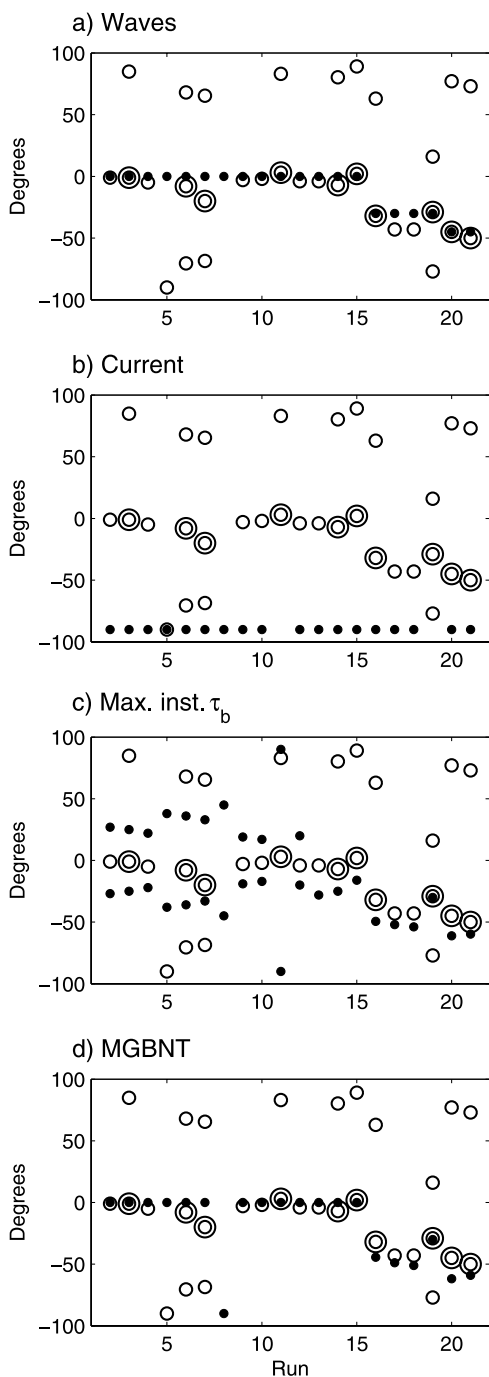


**Figure 17.** Predicted (solid circles) versus observed (open circles) crest orientations for runs 2–7 and 9–21 (no sonar data available for runs 1 or 8). Observations are sonar-derived dominant crest orientations. Double open circles indicate largest of multiple peaks for a given run. In each plot predictions are based on a single mechanism: (a) wave direction, (b) current direction, (c) direction of maximum instantaneous bed shear stress, and (d) direction of MGBNT.

#### 4.2.2. Comparison With Predictions

[50] Dominant ripple crest orientations derived from the sonar images as described in section 3.4 are compared to predictions based on the four potential mechanisms or

factors: the directions of waves, current, maximum instantaneous bed shear stress  $\tau_{b\max}$ , and MGBNT, in Figure 17. The purpose of the comparisons is to evaluate whether any of these mechanisms controlled bed form orientation in these experiments, and which of the factors is the best predictor for bed form orientation. The direction of  $\tau_{b\max}$  was determined from instantaneous  $\tau_b$  estimated as described in section 4.2.1. Observed ripple orientations are in much closer agreement with the predictions based on wave and MGBNT direction than with those based on the direction of the current or  $\tau_{b\max}$ . Although the  $\tau_{b\max}$  predictions correspond well to the observations for the  $60^\circ$  and  $45^\circ$  runs, the lack of symmetric paired observed  $\alpha$  for the  $90^\circ$  runs is a strong indication that, in combined flows, crests do not form solely in response to the  $\tau_{b\max}$ . The comparison between the predictive ability of MGBNT and wave direction is limited by the small number of runs (5) for which these two predictions differ (i.e.,  $\beta < 90$ ). The RMS difference between predicted and measured  $\alpha$  for the five runs with  $\beta < 90$  was  $9.9^\circ$  for MGBNT and  $8.6^\circ$  for waves. In calculating the RMS differences we used the larger peak (indicated by double open circles in Figure 17) for runs with more than two peaks. The RMS of the sonar-derived  $\alpha$  for eight  $90^\circ$  runs was  $4.0^\circ$  (predicted value based on either wave or MGBNT direction is  $0^\circ$ ).

[51] Although wave direction and MGBNT direction are equally good predictors of  $\alpha$  for this data set, MGBNT is the more appealing mechanism theoretically because it addresses the entire transition from pure waves to pure current, in contrast to wave direction alone. The pattern of the  $\alpha$  observations is consistent with the MGBNT predictions, but the predictions overestimate the influence of current. The estimation of sediment transport due to waves and currents required for the MGBNT predictions has a number of uncertainties. The *Meyer-Peter and Muller* [1948] formulation is intended for equilibrium transport; here we apply it to a rapidly varying flow. The role of suspended sediment transport in ripple formation is not accounted for. The phase shift between  $u_w$  and  $\tau_w$  is not included: inclusion of the phase shift would increase the predicted bed form rotation. The estimate of roughness  $k_b$  and its use in GM is uncertain. In addition, bed form orientation may not be in equilibrium at the end of the run: a longer run time may result in more rotation. The tools currently available for predicting sediment transport due to waves and currents are better suited to greater spatial and temporal scales than are relevant to ripple evolution. A numerical model with adequate spatial and temporal resolution and incorporation of the physical processes responsible for bed form evolution could be used to improve confidence in the MGBNT predictions.

[52] The combinations of currents and symmetric waves for which MGBNT predicts significant ( $>10^\circ$ ) rotation of ripple crests are relatively limited (Figure 16). The amount of rotation predicted by MGBNT increases, and rotation can occur for any wave-current angle, when waves are asymmetric. A relatively small degree of asymmetry in the waves in a combined flow can produce significant inequality in transport between the two phases of a wave because transport scales as  $u^3$ . This inequality produces rotation of MGBNT from perpendicular to the waves toward perpendicular to the current. A site characterized by currents

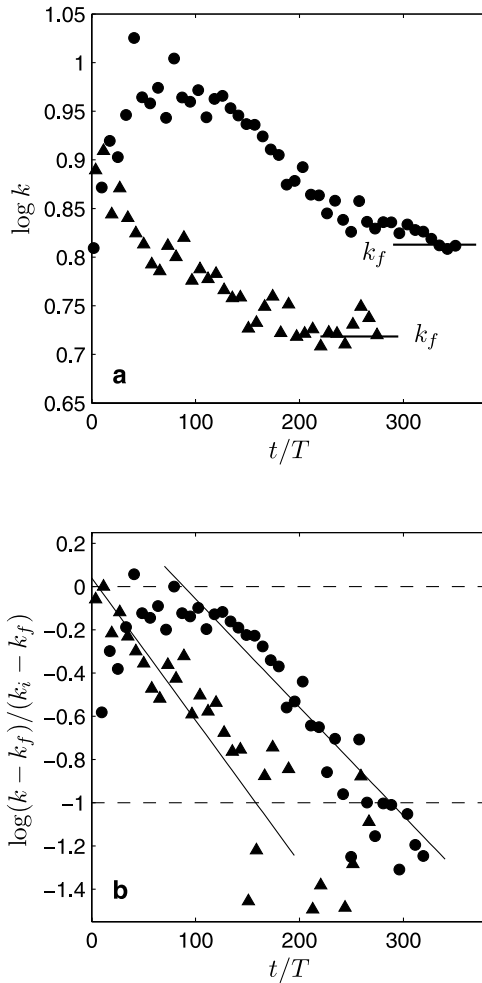


**Figure 18.** (a) Logarithm (base 10) of wave number  $k$  versus number of wave periods. Values used for  $k_f$  shown by horizontal lines. (b) Logarithm of  $(k - k_f)/(k_i - k_f)$  versus number of wave periods and least-square-fit lines for run 9 with  $d_o = 74$  cm and  $\bar{u} = 7$  cm/s (circles) and run 10 with  $d_o = 99$  cm and  $\bar{u} = 7$  cm/s (triangles). Time for evolution to 90% of  $k_f$  is at the intersection of regression lines with dashed line at  $\log[(k - k_f)/(k_i - k_f)] = -1$ .

combined with asymmetric waves, which is typical close to shore, could provide important additional data on the applicability of MGBNT to combined flows.

[53] Although both waves and MGBNT are reasonably good predictors of the largest observed peaks in crest orientation, neither accounts for the development of multiple crest orientations, which we observed in a number of the runs. Some wave-current conditions produce secondary peaks in GBNT, but predicted secondary peaks in GBNT are minimal or nonexistent for the  $\bar{u}$  and  $u_b$  in these 60° and 45° runs. It may not be possible to explain the multiple crests by a single mechanism. For example, in the 90° runs with  $\bar{u}_n = 23$  cm/s that formed bed forms in the wave-current category, one set of crests may be formed by waves and a second by currents.

[54] Although currents did not control bed form orientation for the runs in Figure 17, stronger currents can. Run 8, with  $\bar{u} > 35$  cm/s, was terminated after 17 min because of

excessive downstream loss of sand. The remaining sand formed one large current dune.

### 4.3. Ripple Wavelength Evolution

[55] As ripples grow in response to an increase in wave energy, ripple height  $\eta$  typically increases as an exponential function of the number of wave periods initially, and then the rate of change decreases until  $\eta$  approaches its equilibrium value asymptotically [Smith and Sleath, 2005]. The general form for this pattern of growth is  $\eta(t)/\eta_f = C \exp(-bt/T)$ , where the subscript  $f$  denotes the final or equilibrium value [e.g., Voropayev et al., 1999; Davis et al., 2004; Smith and Sleath, 2005; Doucette and O'Donoghue, 2006]. For vortex ripples it is reasonable to assume that the evolution of  $\lambda$  follows the same pattern as that of  $\eta$ . Faraci and Foti [2002], Doucette and O'Donoghue [2006], and others have found that the evolution time for ripple height and wavelength are similar. To determine the number of wave periods for  $\lambda$  to evolve to 90% of its equilibrium value for each run, we used the expression from Smith and Sleath [2005] for evolution of ripple wave number  $k = 1/(2\pi\lambda)$ :

$$\frac{k - k_f}{k_i - k_f} = C \exp(-bt/T) \quad (4)$$

where the subscript  $i$  denotes initial wave number. Smith and Sleath developed this equation for a transition in ripple morphology due to a change in wave energy. As most of our runs started from flat bed, we applied equation (4) to the transition from the initial ripples resolved by the sonar to the final bed state.

[56] Here  $k_f$  was estimated as the average value after wave number stopped decreasing steadily (Figure 18a). The  $k_f$  frequently was reached close to the end of the run, increasing the uncertainty in its value. The  $k_i$  was taken as either the maximum value or the average value before exponential decay began. The least-squares-fit line between  $\log[(k - k_f)/(k_i - k_f)]$  and number of wave periods  $t/T$  was found for the portion of the data that exhibited exponential decay in wave number (Figure 18b), following equation (4). The average coefficient of determination  $R^2$  for 15 runs was 0.77 (s.d. 0.14). For some runs producing three-dimensional bed forms  $R^2$  was less than 0.5 and evolution time was not estimated.

[57] Two measures of nondimensionalized evolution time  $t/T$  were calculated. We denote the number of wave periods from the beginning of the run to 90% evolution ( $\log[(k - k_f)/(k_i - k_f)] = 0.1$ ) by  $n_e$ , and from the beginning of wave number decay ( $t/T$  corresponding to  $k_i$ ) to 90% evolution by  $n_g$ . The average  $n_e$  for 15 runs was 160 (s.d. 47), and the average  $n_g$  was 126 (s.d. 45) (Table 2). The  $n_e$  and  $n_g$  were

**Table 2.** Number of Wave Periods for Evolution to 90% of Equilibrium Wavelength for 2D (Categories LR or IR) and 3D (Categories WC, T, or 3D) Bed Forms

	$n_e$		$n_g$		$N$
	Mean	s.d.	Mean	s.d.	
All types	160	47	126	45	15
2D from flat bed	184	49	154	38	7
2D transitions	156	47	119	45	3
3D from flat bed	129	30	91	32	5

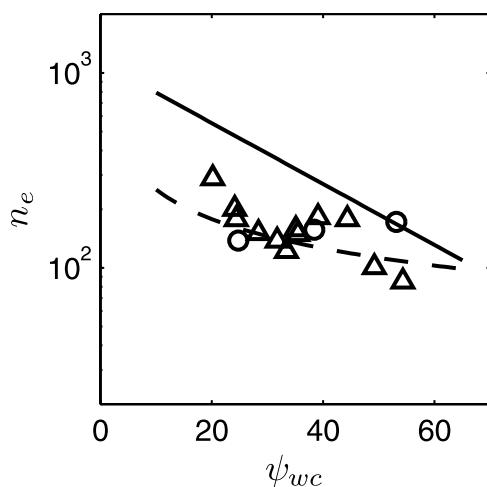


**Figure 19.** Total number of wave periods for wavelength to evolve to 90% of final wavelength ( $n_e$ ) versus wave-current mobility number. Triangles are runs starting from flat bed and circles are transition runs (2–4). Solid line is relationship proposed by *Doucette and O'Donoghue* [2006]; dashed line is relationship proposed by *Voropayev et al.* [1999].

not significantly less for the transition runs than for development of 2D ripples from flat bed (note small  $N$ ), consistent with the finding of *Doucette and O'Donoghue* [2006] that  $n_e$  does not vary with initial bed state. Average  $n_e$  and  $n_g$  were less for 3D than for 2D bed form categories, suggesting that bed morphology influences the processes that build bed forms, for example by altering near-bed velocities, turbulence, and the bed shear stress responsible for bedload transport.

[58] The  $n_e$  (and thus  $-b$  in equation (4)) decreases with increasing  $\psi_{wc}$  (Figure 19). This type of relationship between  $n_e$  and  $\psi$  or the Shields parameter has been observed previously [*Voropayev et al.*, 1999; *Davis et al.*, 2004; *Smith and Sleath*, 2005; *Doucette and O'Donoghue*, 2006], and several different forms for the relationship have been proposed. Our results correspond more closely to the expression for  $n_e$  as a function of  $\psi$  proposed by *Voropayev et al.* [1999] than to that proposed by *Doucette and O'Donoghue* [2006]. *Doucette and O'Donoghue's* expression for growth to 95% of equilibrium has been adjusted to estimate 90% of equilibrium in Figure 19 for comparison with our  $n_e$ .

[59] The difference between  $n_e$  and  $n_g$ , or the number of wave periods before exponential growth began, varied considerably among runs. The long interval before growth of  $\lambda$  commenced in certain runs (Figure 18b) may indicate that, in these cases, the first ripples to appear were rolling-grain ripples. According to *Sleath* [1984], waves over a flat bed initially form rolling-grain ripples, which are created entirely by bedload transport. Vortex ripples develop subsequently, as ripple height and steepness increase. Rolling-grain ripples have been observed in laboratory experiments but their existence in the field is disputed [*Miller and Komar*, 1980]. *Faraci and Foti* [2002] found in experiments in a wave tank with regular waves that rolling-grain ripples (characterized by steepness  $\sim 0.1$ ) developed initially and

evolved into vortex ripples after 100–200 s ( $1.5 \text{ s} < T < 4.2 \text{ s}$ ). Our runs that had delayed ripple growth, suggesting a transient stage of rolling-grain ripples, were characterized by small waves and slow currents.

## 5. Conclusions

[60] Experiments were conducted with an oscillating plate in a 4-m-wide flume to investigate the morphology and evolution of ripples formed by waves and currents. Increasing the ratio of current to wave velocity influenced bed forms in two ways. First, higher ratios of current to wave energy created more three-dimensional bed forms. Ratios of  $u_{*c}/u_{*w} < 0.55$  produced linear or irregular wave ripples, while  $u_{*c}/u_{*w} > 0.55$  produced superimposed wave and current ripples or tiled bed forms. Second, stronger currents decreased ripple height and wavelength. The decrease in ripple dimensions is largely explained by the increase in fluid excursion and maximum velocity produced by the addition of current. The  $d_o/D$  in the experiments bracketed the value for the predicted transition from orbital to suborbital ripples [*Wiberg and Harris*, 1994]. When a length scale  $d_{wc}$  that takes into account the combined wave-current excursion is substituted for  $d_o$ , predicted ripple type changes from orbital to suborbital and predicted ripple wavelength decreases.

[61] Bed form evolution was documented by sonar images collected throughout the runs. The first wavelengths to appear in sonar images were typically 8–12 cm. Initial growth of ripple wavelength was exponential. The number of wave periods for ripple wavelength to reach 90% of equilibrium value ( $n_e$ ) decreased with increasing wave-current mobility number. Average  $n_e$  was 184 for 2D ripples ( $N = 7$ ) and 129 for 3D ripples ( $N = 5$ ), starting from a flat bed. The average  $n_e$  for transition from one equilibrium rippled bed to another due to change in wave forcing was 156 ( $N = 3$ ). In runs with wave mobility number less than 26 and currents of 0–7 cm/s, exponential growth was preceded by a 40–60 wave-period interval of no detectable growth. We hypothesize that in these runs, the initial ripples were rolling-grain ripples, and that during the interval of no growth they developed into vortex ripples.

[62] The dominant orientations of bed form crests at the end of the runs were compared to predicted orientation based on four potential controlling mechanisms: the directions of waves, current, maximum instantaneous wave-current bed shear stress  $\tau_{wc}$ , and maximum gross bed normal transport (MGBNT). Maximum instantaneous  $\tau_{wc}$  and current were eliminated as controlling mechanisms for bed form orientation. Observed orientations correspond closely to predictions based on wave and MGBNT directions. More data are required to determine which of these two mechanisms is a better predictor of orientation.

[63] **Acknowledgments.** The experiments could not have been completed without the assistance of Hideo Iijima and Kazuhiro Yuhora of the Terrestrial Environment Research Center (TERC) at the University of Tsukuba. Kevin O'Toole (USGS) was instrumental in the design, manufacture, and assembly of the oscillating plate system. Thanks go to Gerry Hatcher (USGS) who was always willing to help get things to work, and to the staff and students of TERC for their assistance and hospitality during our stay in Japan. Chris Sherwood and Jingping Xu of the USGS and two anonymous reviewers provided helpful comments on the manuscript. This work was supported by the Office of Naval Research Coastal Geosciences

Program Ripples DRI and the USGS Coastal and Marine Geology Program. Any use of trade, product, or firm names in this paper is for descriptive purposes only and does not imply endorsement by the U.S. government.

## References

- Amos, C. L., A. J. Bowen, D. A. Huntley, and C. F. M. Lewis (1988), Ripple generation under combined influences of waves and currents on the Canadian continental shelf, *Cont. Shelf Res.*, *8*, 1129–1153.
- Andersen, K. H., and C. Faraci (2003), The wave plus current flow over vortex ripples at an arbitrary angle, *Coastal Eng.*, *47*(4), 431–441, doi:10.1016/S0378-3839(02)00158-8.
- Bagnold, R. A. (1946), Motion of waves in shallow water: Interactions of waves and sand bottoms, *Proc. R. Soc., Ser. A*, *187*, 1–15.
- Cataño Lopera, Y. A., and M. H. Garcia (2006), Geometry and migration characteristics of bedforms under waves and currents. part 2: Ripples superimposed on sandwaves, *Coastal Eng.*, *53*(9), 781–792, doi:10.1016/j.coastaleng.2006.03.008.
- Clifton, H. E., and J. R. Dingle (1984), Wave-formed structures and paleoenvironmental reconstruction, *Mar. Geol.*, *60*, 165–198.
- Davis, J. P., D. J. Walker, M. Townsend, and I. R. Young (2004), Wave-formed sediment ripples: Transient analysis of ripple spectral development, *J. Geophys. Res.*, *109*, C07020, doi:10.1029/2004JC002307.
- Doucette, J. S., and T. O'Donoghue (2006), Response of sand ripples to change in oscillatory flow, *Sedimentology*, *53*, 581–596, doi:10.1111/j.1365-3091.2006.00774.x.
- Dumas, S., R. Arnott, and J. B. Southard (2005), Experiments on oscillatory-flow and combined-flow bed forms: Implications for interpreting parts of the shallow-marine sedimentary record, *J. Sediment. Res.*, *75*(3), 501–513, doi:10.2110/jsr.2005.039.
- Faraci, C., and E. Foti (2002), Geometry, migration and evolution of small-scale bedforms generated by regular and irregular waves, *Coastal Eng.*, *47*(1), 35–52.
- Gallagher, E. L., S. Elgar, and E. B. Thornton (1998), Megaripple migration in a natural surf zone, *Nature*, *394*, 165–168.
- Grant, W. D., and O. S. Madsen (1979), Combined wave and current interaction with a rough bottom, *J. Geophys. Res.*, *84*(C4), 1797–1808.
- Grant, W. D., and O. S. Madsen (1982), Movable bed roughness in unsteady oscillatory flow, *J. Geophys. Res.*, *87*(C1), 469–481.
- Grasmeijer, B. T., and M. G. Kleinans (2004), Observed and predicted bed forms and their effect on suspended sand concentrations, *Coastal Eng.*, *51*, 351–371, doi:10.1016/j.coastaleng.2004.05.001.
- Hanes, D. M., V. Alymov, Y. S. Chang, and C. Jette (2001), Wave-formed sand ripples at Duck, North Carolina, *J. Geophys. Res.*, *106*(C10), 22,575–22,592.
- Hansen, J., M. van Hecke, A. Haaning, C. Ellegaard, K. Andersen, T. Bohr, and T. Sams (2001), Pattern formation: Instabilities in sand ripples, *Nature*, *410*, 324.
- Khelifa, A., and Y. Ouellet (2000), Prediction of sand ripple geometry under waves and currents, *J. Waterw. Port Coastal Ocean Eng.*, *126*(1), 14–22.
- Kocurek, G., and R. C. Ewing (2005), Aeolian dune field self-organization—Implications for the formation of simple versus complex dune-field patterns, *Geomorphology*, *72*, 94–105.
- Lee Young, J., and J. Sleath (1990), Ripple formation in combined trans-directional steady and oscillatory flow, *Sedimentology*, *37*, 509–516.
- Li, M. Z., and C. L. Amos (1998), Predicting ripple geometry and bed roughness under combined waves and currents in a continental shelf environment, *Cont. Shelf Res.*, *18*, 941–970.
- Madsen, O. S. (1991), Mechanics of cohesionless sediment transport in coastal waters, in *Coastal Sediments '91*, vol. 1, edited by N. C. Kraus, K. J. Gingerich, and D. L. Kriebel, pp. 15–27, Am. Soc. of Civ. Eng., Reston, Va.
- Madsen, O. S. (1994), Spectral wave-current bottom boundary layer flows, paper presented at 24th International Conference on Coastal Engineering, Am. Soc. of Civ. Eng., Reston, Va.
- Manohar, M. (1955), Mechanics of bottom sediment movement due to wave action, *Beach Erosion Board Tech. Memo. 75*, U.S. Army Corps of Eng., Washington, D. C.
- Mardia, K. V. (1972), *Statistics of Directional Data*, Academic Press, London.
- Meyer-Peter, E., and R. Muller (1948), Formulas for bed-load transport, paper presented at 2nd Congress of the IAHR, Int. Assoc. of Hydrol. Eng. and Res., Madrid.
- Miller, M. C., and P. D. Komar (1980), Oscillation sand ripples generated by laboratory apparatus, *J. Sediment. Petrol.*, *50*(1), 173–182.
- Mogridge, G. R., M. Davies, and D. Willis (1994), Geometry prediction for wave-generated bedforms, *Coastal Eng.*, *22*(C11), 255–286, doi:10.1016/0378-3839(94)90039-6.
- Nielsen, P. (1981), Dynamics and geometry of wave-generated ripples, *J. Geophys. Res.*, *86*(C7), 6467–6472.
- Nielsen, P. (1992), *Coastal Bottom Boundary Layers and Sediment Transport*, World Sci., Hackensack, N. J.
- Nishimori, H., M. Yamasaki, and K. H. Andersen (1998), A simple model for the various pattern dynamics of dunes, *Int. J. Mod. Phys. B*, *12*(3), 257–272.
- O'Donoghue, T., and G. S. Clubb (2001), Sand ripples generated by regular oscillatory flow, *Coastal Eng.*, *44*(2), 101–115.
- O'Donoghue, T., J. S. Doucette, J. J. van der Werf, and J. S. Ribberink (2006), The dimensions of sand ripples in full-scale oscillatory flows, *Coastal Eng.*, *53*(12), 997–1012, doi:10.1016/j.coastaleng.2006.06.008.
- Osborne, P. D., and C. E. Vincent (1993), Dynamics of large and small scale bedforms on a macrotidal shoreface under shoaling and breaking waves, *Mar. Geol.*, *115*, 207–226.
- Rubin, D. M., and R. E. Hunter (1987), Bedform alignment in directionally varying flows, *Science*, *237*, 276–278.
- Rubin, D. M., and H. Ikeda (1990), Flume experiments on the alignment of transverse, oblique, and longitudinal dunes in directionally varying flows, *Sedimentology*, *37*, 673–684.
- Sleath, J. F. A. (1975), A contribution to the study of vortex ripples, *J. Hydraul. Res.*, *13*, 315–328.
- Sleath, J. F. A. (1978), Measurements of bed load in oscillatory flow, *J. Waterw. Port Coastal Ocean Eng.*, *104*(WW4), 291–307.
- Sleath, J. F. A. (1984), *Sea Bed Mechanics*, John Wiley, Hoboken, N. J.
- Sleath, J. (1990), Velocities and bed friction in combined flows, paper presented at 22nd Conference on Coastal Engineering, Am. Soc. of Civ. Eng., Reston, Va.
- Sleath, J. F. A. (1991), Velocities and shear stresses in wave-current flows, *J. Geophys. Res.*, *96*(C8), 15,237–15,244.
- Smith, D., and J. F. A. Sleath (2005), Transient ripples in oscillatory flow, *Cont. Shelf Res.*, *25*, 485–501.
- Smyth, J., and M. Li (2005), Wave-current bedform scales, orientation, and migration on sable island bank, *J. Geophys. Res.*, *110*(C2), C02023, doi:10.1029/2004JC002569.
- Styles, R., and S. M. Glenn (2002), Modeling bottom roughness in the presence of wave-generated ripples, *J. Geophys. Res.*, *107*(C8), 3110, doi:10.1029/2001JC000864.
- Traykovski, P., A. E. Hay, J. D. Irish, and J. E. Lynch (1999), Geometry, migration, and evolution of wave orbital ripples at LEO-15, *J. Geophys. Res.*, *104*(C1), 1505–1524.
- Voropayev, S., G. McEachern, D. Boyer, and H. Fernando (1999), Dynamics of sand ripples and burial/scouring of cobbles in oscillatory flow, *Appl. Ocean Res.*, *21*, 249–261.
- Werner, B. (1995), Eolian dunes: Computer simulations and attractor interpretation, *Geology*, *23*(12), 1107–1110.
- Wiberg, P. L., and C. K. Harris (1994), Ripple geometry in wave-dominated environments, *J. Geophys. Res.*, *99*(C1), 775–789.
- Williams, J. J., P. S. Bell, and P. D. Thorne (2005), Unifying large and small wave-generated ripples, *J. Geophys. Res.*, *110*, C02008, doi:10.1029/2004JC002513.
- Xu, J. P., and L. D. Wright (1995), Test of bed roughness models using field data from the Middle Atlantic Bight, *Cont. Shelf Res.*, *15*, 1409–1434.

D. M. Hanes, J. R. Lacy, and D. M. Rubin, U.S. Geological Survey, Pacific Science Center, 400 Natural Bridges Drive, Santa Cruz, CA 95060, USA. (jlacy@usgs.gov)

H. Ikeda and K. Mokudai, Terrestrial Environment Research Center, University of Tsukuba, Tsukuba, Ibaraki 305-8577, Japan.